4. EXPERIMENTAL REPORTS

DEPARTMENT OF NEUTRON INVESTIGATION OF CONDENSED MATTER

Theoretical and experimental study of elastic wave propagation in anisotropic texurized rocks
A.N.Nikitin, V.K.Ignatovich, T.I.Ivankina, A.A.Kruglov, T.Lokajicek, L.T.N.Phan and R.N.Vasin

Структурные аномалии pr-содержащих оксидов при низких температурах
А.М. Балагуров, И.А. Бобриков, В.Ю. Помякушин, Е.В. Помякушина, Д.В. Шептяков, И.О.Троянчук

Nucleation theory models for describing kinetics of cluster growth in C60/NMP solutions
T.V. Tropin, M.V. Avdeev, O.A. Kyzyma, V.L. Aksenov

Solvatochromism in fullerene solutions
T.A.Kyrey, O.A.Kyzyma , M.V.Avdeev, V.L.Aksenov, M.V.Korobov, L.A.Bulavin

Sans study of water-based ferrofluids for brain cancer therapy
M.V.Avdeev, A.V.Feoktystov, B.Mucha, V.M.Garamus, R.Willumeit, K.Lamszus, L.Vekas, O.Marinica, R.Turcu

Observation of non-specular neutron reflection from a magnetic film placed in oscillating magnetic field
S.V. Kozhevnikov, V.K. Ignatovich, Yu.V. Nikitenko, F. Radu, A. Rühm and J. Major

Ultrasonic treatment effect on the long-term stability of biogenic ferrihydrite nanoparticles samples in aqueous solution under ambient conditions
M. Balasoiu, L. Anghel, A. V. Rogachev, L.A. Ishchenko, A. Jigounov, G.M. Arzumanian, S.V. Stolyar, R.S. Iskhakov, Yu.L. Raikher

Structural and magnetic phase transitions in multiferroic BiMnO3 at high pressures
D.P.Kozlenko, A.A.Belik, S.E.Kichanov, D.V.Sheptyakov, Th.Straessle and B.N.Savenko

A study of cluster formation in silicon glasses doped by TiO_2/CeO_2 oxides.
S.E.Kichanov, S.A.Samoylenko, D.P.Kozlenko, A.V.Belushkin, L.A.Bulavin, G.P.Shevchenko, V.C.Gurin, V.Haramus and B.N.Savenko

Morphology of the phospholipid transport nanosystem
M.A. Kiselev, E.V. Ermakova, O.M. Ipatova, A.V. Zabelin

Метод след-отображения для решетки пела
Эльмар Аскеров

Results of measurement the residual strains in the WWER-1000 reactor vessel
V.V.Sumin, A.M.Balagurov , I.V.Papushkin , R. Wimpory

The resolution function of a tof reflectometer in the gravity field
I. Bodnarchuk, S.Manoshin, S.Yaradaikin, V.Kazimirov, and V.Bodnarchuk

Aqueous solutions of poly(ethylene glycol): SANS study
G.Lancz, M.V.Avdeev, V.I.Petrenko, V.M.Garamus, M.Koneracká and P.Kopčanský

Contrast variation in small-angle neutron scattering on water-based magnetic fluid with sodium oleate and polyethylene glycol stabilization
M.V.Avdeev, A.V.Feoktystov, P.Kopcansky, G.Lancz, M.Timko, M.Koneracka, V.Zavisova, N.Tomasovicova, A.Jurikova, K.Csach, V.M.Garamus, R.Willumeit, L.A.Bulavin

DEPARTMENT OF IBR-2 SPECTROMETERS COMPLEX

Создание макета технологической системы криогенного замедлителя с электроникой управления и контроля
Ананьев В.Д., Беляков А.А., Богдзель А.А., Булавин М.В., Верхоглядов А.Е., Кулагин Е.Н., Куликов С.А., Кустов А.А., Мухин К.А., Петухова Т.Б., Сиротин А.П., Федоров А.Н., Шабалин Е.П., Шабалин Д.Е., Широков В.К.

NUCLEAR PHYSICS DEPARTMENT

Epithermal neutron activation analysis of the asian herbal plants
Baljinnyam N., Jugder B., Norov N., Frontasyeva M.V.,Ostrovnaya T.M., S.S. Pavlov

Radiometry of ^{137}Cs and ^{210}Pb in moss from belarus
Aleksiayenak Yu. V., Frontasyeva M.V., Florek M., Faanhof A.

THEORETICAL AND EXPERIMENTAL STUDY OF ELASTIC WAVE PROPAGATION IN ANISOTROPIC TEXURIZED ROCKS

A.N.Nikitin[a], V.K.Ignatovich[a], T.I.Ivankina[a], A.A.Kruglov[a], T.Lokajicek[b], L.T.N.Phan[c] and R.N.Vasin[a]

[a] Frank Laboratory of Neutron Physics, Joint Institute for Nuclear Research, DubnaбRussia
[b] Institute of Geology, Academy of Sciences of the Czech Republic, Prague, Czech Republic
[c] Tula State University, Tula, Russia

Theoretical and experimental investigations of elastic wave propagation in a bilayer media have been provided. It was shown that elastic waves of quasi-longitudinal and quasi-transverse polarizations propagate through axial anisotropic media. Wave reflection from a free surface is in general accompanied by triple splitting and all the reflected waves are nonspecular. The quasi-longitudinal and quasi-transverse elastic waves contain the both longitudinal and transverse constituents. This fact may be a reason for the discrepancy which did not observed in the elasticity theory earlier.

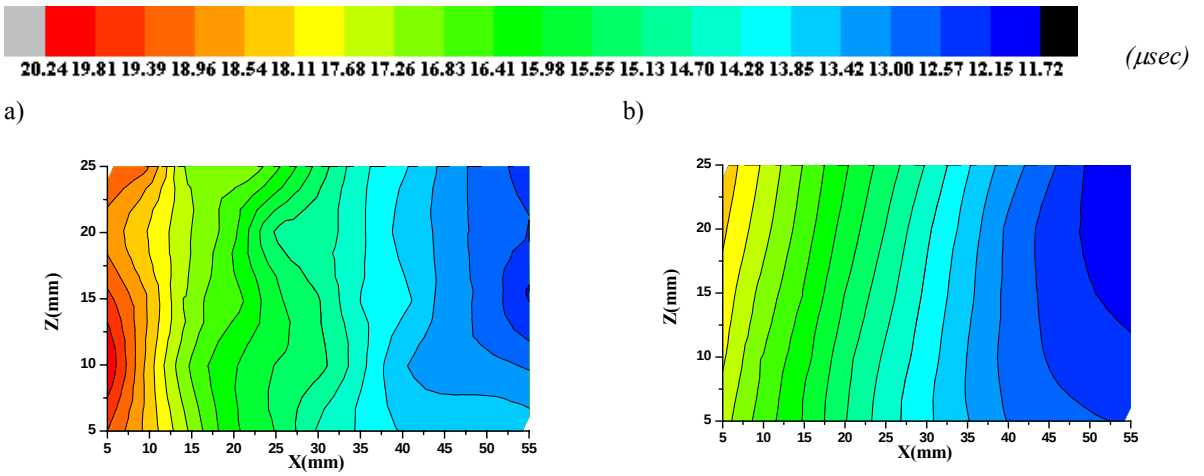

Fig 1. The map of the isoline disctribution of traveltimes of the quasi-longitudinal wave passed through the model – "plexiglas – quartz". The **XZ** plane of the single quartz coincides with the plexiglas surface. The transmitter is fixed on the plexiglas face at the angle of 60° to the horizontal surface. a) ultrasounic frequency - 200 кHz; b) ultrasounic frequency - 5 мHz.

For example, it was found out that even for isotropic medium the reflection of shear wave from an interface having the polarization in the incidence plane can create non Rayleigh longitudinal surface wave which can accumulate devastating amounts of energy at the critical grazing angle. Moreover, the energy density of surface wave may hundred times exceed the energy density of the incident elastic wave. The observed result is very important for seismology.

To improve the considered model and to check the reliability of results we performed the study of elastic wave propagation through model isotropic-anisotropic medium. A set of samples of different compositions were investigated («plexiglas + single quartz oriented parallel to the optical axis», «plexiglas + single quartz oriented perpendicular to the optical axis», «plexiglas + polycrystalline graphite (with certain texture)», «epoxy + biotite»). Crystallographic texture of graphite was determined by means of neutron diffraction.

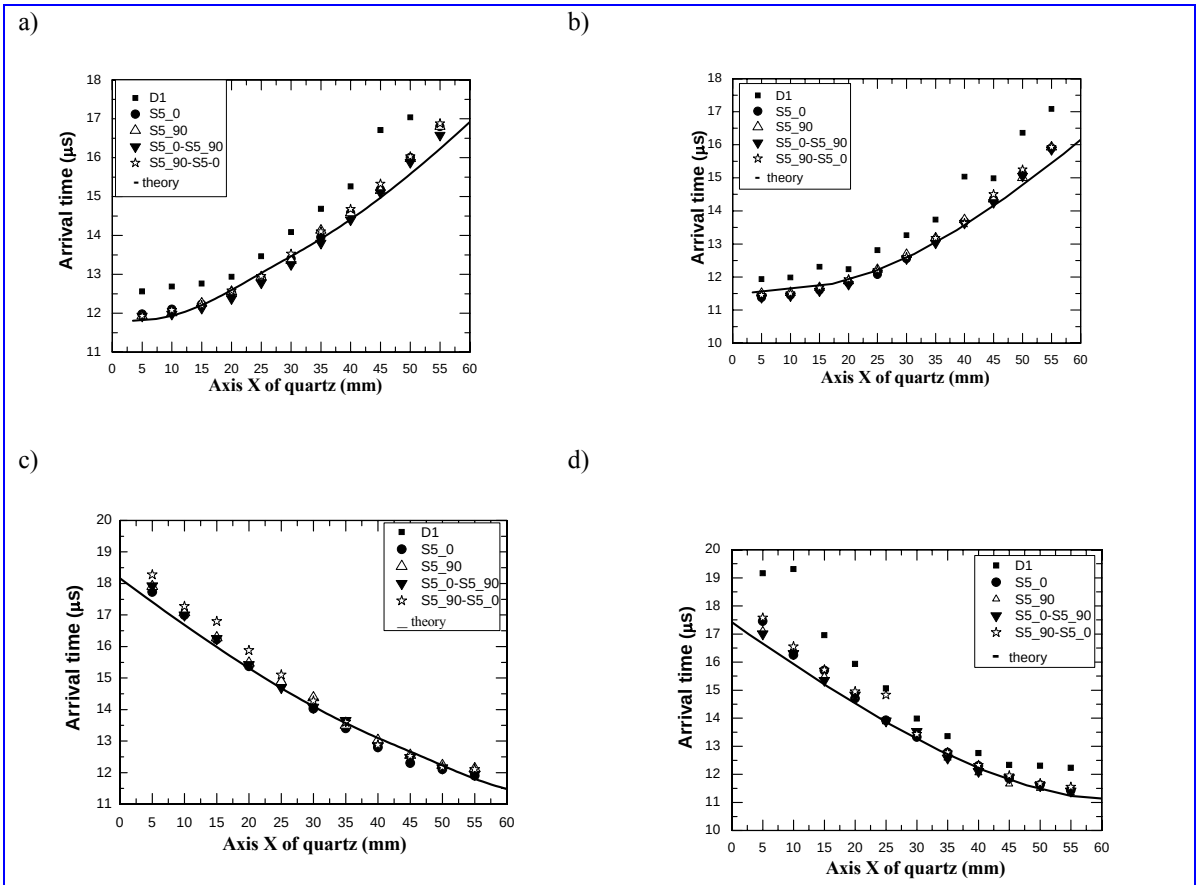

Fig. 2. The comparison of experimental values of arrival time of quasi-longitudinal wave reached the top quartz surface with calculated values. The direction of incident longitudinal wave occurs (a, b) at the angle of 30° to the quartz **XZ** plane; (c, d) at the angle of 60° to the quartz **XY** plane.

Elastic waves were generated by piezoelectric transmitters which are fixed in a certain point of the isotropic part of the sample. The receiver was scanning the surface of the quartz bar (anisotropic part). We registered the wave patterns of the mixed quasi-longitudinal and quasi-transverse elastic waves of different frequencies passing through the investigated samples in depend on grazing angle of the propagating elastic wave in respect to the interface (or to the foliation) **(Figure 1)**.

The comparison between calculated and measured data of quasi-longitudinal waves came to the satisfactory agreement **(Figure 2).**

СТРУКТУРНЫЕ АНОМАЛИИ PR-СОДЕРЖАЩИХ ОКСИДОВ ПРИ НИЗКИХ ТЕМПЕРАТУРАХ

А.М. Балагуров[a], И.А. Бобриков[a], В.Ю. Помякушин[b], Е.В. Помякушина[b], Д.В. Шептяков[b], И.О.Троянчук[c]

[a] Объединенный институт ядерных исследований, Дубна, Россия
[b] Laboratory for Neutron Scattering, Paul Scherrer Institute, Switzerland
[c] Объединенный институт твердого тела и полупроводников, Минск, Белоруссия

В исследованиях сложных оксидов переходных металлов (манганитов и кобальтитов) типа $A_{1-x}A'_xBO_3$, где A - редкоземельный элемент, A′ - щелочноземельный элемент, B = Mn или Co, выбор того или иного редкоземельного элемента или комбинации нескольких разных элементов сводится, как правило, к желанию подобрать необходимую величину среднего радиуса A-катиона, $\langle r_A \rangle$, которая во многом определяет физические свойства соединения. Однако еще в исследованиях ВТСП было замечено, что соединения с празеодимом ведут себя иначе, чем с другими редкоземельными элементами, причем аномальное поведение Pr-содержащих перовскитов, обычно проявляется при сравнительно низких температурах. Для сложных оксидов марганца и кобальта на особые свойства составов с Pr внимание было обращено сравнительно недавно, но уже накоплен необходимый для анализа экспериментальный материал. Так, магнитные исследования состава $Pr_{0.5}Sr_{0.5}CoO_3$, (далее PSCO) показали [**1**], что в нем наблюдаются два фазовых перехода при $T_C \approx 226$ K и $T_A \approx 120$ K, тогда как в соединениях с другими редкоземельными катионами есть только один высокотемпературный переход, при котором возникает ферромагнитное упорядочение. В составе $Pr_{0.5}Ca_{0.5}CoO_3$ в работе [**2**], при $T \approx 75$ K обнаружены аномалии физических свойств (переход метал – изолятор) и заметная перестройка структуры, которые отсутствуют в составе $La_{1/6}Nd_{1/3}Ca_{0.5}CoO_3$, имеющем такой же средний радиус A-катиона. В соединении $PrAlO_3$, в котором нет каких-либо магнитных переходов, обнаружена сходная с PSCO последовательность структурных переходов и аномалия в упругих свойствах при 118 K [**3**].

Таким образом, есть основания считать, что наблюдающиеся в соединениях с Pr низкотемпературные аномалии в физических свойствах связаны с общей причиной, а именно, с формированием новых устойчивых химических связей и следует искать структурные проявления этого эффекта. В принципе, они уже были найдены в нашей недавней работе [**4**], где было показано, что данные, полученные с помощью дифракции синхротронного излучения и особенно нейтронов с очень высоким разрешением, позволяют утверждать, что в PSCO при T_A происходит изменение симметрии кристалла. Экспериментальные результаты, представленные в [**4**], носили предварительный характер и относились только к геометрии кристаллической решетки. В дальнейших более детальных дифракционных экспериментах нам удалось получить информацию об атомной и магнитной структуре PSCO в области низких температур. Анализ всех имеющихся данных позволяет утверждать, что в $Pr_{0.5}Sr_{0.5}CoO_3$ при температурах ниже 170 K происходит расслоение кристалла на две фазы с разной симметрией и разными (хотя и близкими) атомной и магнитной структурами. Основным структурным различием между фазами является конфигурация кубооктаэдра $(Pr,Sr)O_{12}$, а наблюдавшаяся в предыдущих работах при 120 K магнитная аномалия является следствием перестройки кислородного окружения (Pr,Sr) и, в некоторой степени, Co.

Литература

1. И.О. Троянчук и др., Письма в ЖЭТФ **84**, 180 (2006).
2. A.J. Barón-González et al., Phys. Rev. B **81**, 0544427 (2010).
3. M.A. Carpenter et al., Phys. Rev. **B 72**, 024118 (2005).
4. А.М. Балагуров, И.А. Бобриков, Д.В. Карпинский, И.О. Троянчук, В.Ю. Помякушин, Д.В. Шептяков, Письма в ЖЭТФ **88**, 608 (2008).

NUCLEATION THEORY MODELS FOR DESCRIBING KINETICS OF CLUSTER GROWTH IN C_{60}/NMP SOLUTIONS

T.V. Tropin[a], M.V. Avdeev[a], O.A. Kyzyma[a,b], V.L. Aksenov[a,c]

[a] *Frank Laboratory of Neutron Physics, Joint Institute for Nuclear Research, Dubna, Russia*
[b] *Kyiv Taras Shevchenko National University, Kyiv, Ukraine*
[c] *Russian Research Centre "Kurchatov Institute", Moscow, Russia*

In the given report, two kinetic models of cluster growth, based on nucleation theory approach are applied to describe cluster growth in C_{60}/N-methyl-pyrrolidone (NMP) solutions. As compared to low-polarity C_{60} solutions, where fullerenes show a tendency towards aggregation under supersaturation as a result of non-equilibrium dissolution [1], in polar solvents, like NMP, fullerenes C_{60} always form clusters. Particularly, in pyridine [2], NMP [3] and their mixtures with water [1] clusters grow up to 500 nm in size during about one month after fullerene dissolution.

For the spectrum from the initial solution specific features of molecular state of C_{60} can be seen (e.g. peak at λ=330nm). The UV-Vis spectrum from C_{60}/NMP changes with time **(Fig. 1)**, which is known as temporal solvatochromism. The absorption measurements can be used for determination of the free (non-aggregated) fullerene concentration in C_{60}/NMP at different time after the solution preparation. For this purpose fullerene is extracted into a solvent, which dissolves C_{60} and is non-miscible with NMP. The good solvent for such procedure is hexane. The time dependence of free monomer concentration in C_{60}/NMP found in this way is shown in **Fig. 1**. It decreases by more than three orders in comparison with initial solution, which means that fullerene in the "old" NMP solution is mainly in cluster state (free monomer concentration $c_{mon}<10^{-3}$ mg/ml). It is important to note that estimates of cluster density made by SANS at the addition of water to C_{60}/NMP [6] indicate that clusters are fullerene molecular crystallites.

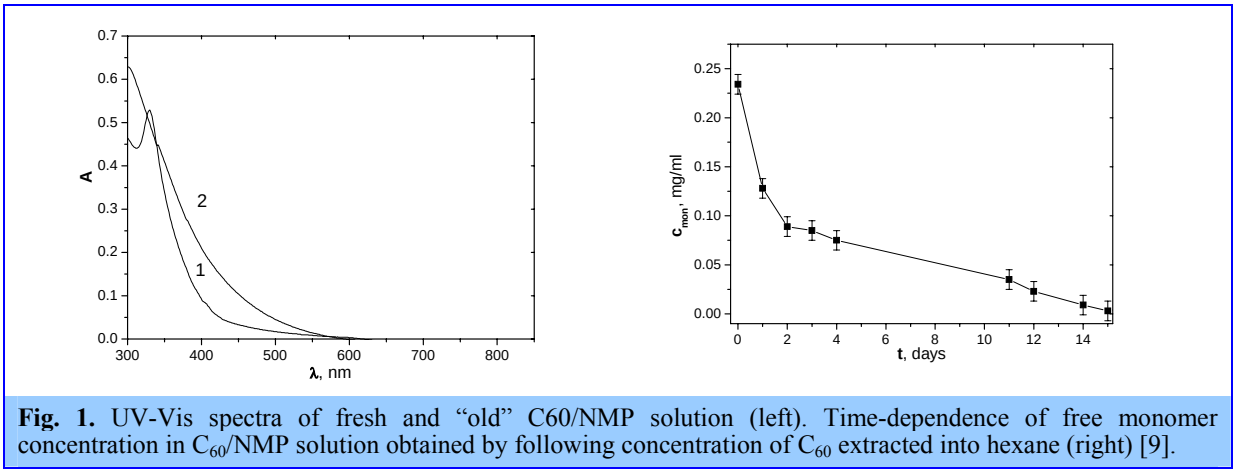

Fig. 1. UV-Vis spectra of fresh and "old" C60/NMP solution (left). Time-dependence of free monomer concentration in C_{60}/NMP solution obtained by following concentration of C_{60} extracted into hexane (right) [9].

Basics of aapplication of nucleation theory for describing fullerene cluster formation are described elsewhere [1,4]. Evolution of a system in frame of classical nucleation theory, described by liquid drop model, results in phase separation, when all but c_{eq} of free molecules, transfer finally to the solid phase (infinite cluster). Because this is not the case for fullerene polar solutions, where clusters stay stable for long periods of time, one should consider new models. Taking into account a possible appearance of some new chemical bonds, which stabilize clusters in this type of solutions, the corresponding modifications of kinetic equations can be done in two ways.

In the first case (model I), we introduce an additional function $f^{*}(n,t)$, which describes clusters excluded at the moment t from the nucleation process (segregating phase). The size of these clusters is strongly stabilized and does not change furthermore. It is clear that finally the segregating phase transfers completely into the stabilized phase. The basic equations for this model take the form:

$$\frac{\partial f(n,t)}{\partial t} = w^{(+)}_{n-1,n} f(n-1,t) + w^{(-)}_{n+1,n} f(n+1,t) - w^{(+)}_{n,n+1} f(n,t) - (w^{(-)}_{n,n-1} + \frac{1-e^{t/\tau}}{\tau}) f(n,t),$$

$$\frac{\partial f'(n,t)}{\partial t} = \frac{1-e^{t/\tau}}{\tau} f(n,t), \quad \sum_{n=1}^{\infty} n(f(n,t) + f'(n,t)) = c, \qquad (1)$$

$$f(n,t=0) = \begin{cases} 0, & n>1, \\ c, & n=1. \end{cases} \quad f'(n,t=0) = 0.$$

Where the additional term in the kinetic equations for $f(n,t)$ corresponds to exponential depletion of the segregating phase. The new model parameter, τ, is the characteristic time of cluster stabilization.

In the other case (model II), kinetic equations keep the classical form [1,4], but probabilities of cluster growth / depletion $w^{(\pm)}_{m,n}$ are the functions of time:

$$w^{(\pm)}_{m,n}(t) = w^{(\pm)}_{m,n} e^{-t/\tau}, \qquad (2)$$

where the characteristic time τ reflects a decrease in the nucleation rate.

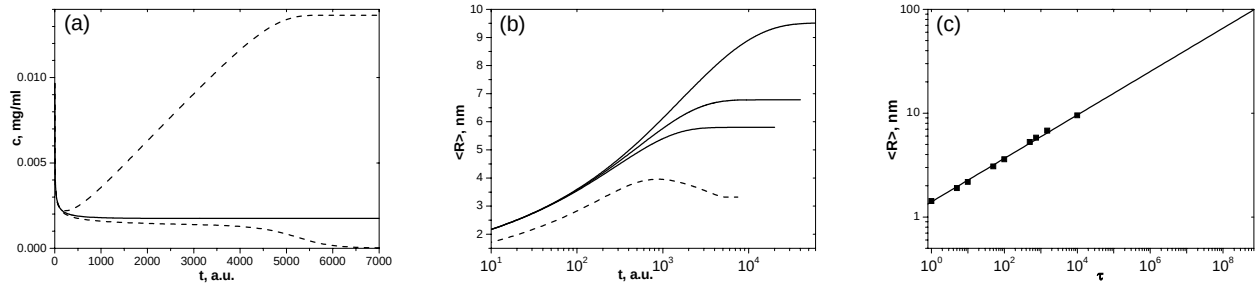

Fig. 2. (*a*) time evolution of monomer concentration for both models I (dashed lines) and II (solid line). For model I the upper curve shows the sum $f(1,t)+f'(1,t)$; and the lower curve shows $f(1,t)$; (*b*) evolution of mean cluster size for models I (dashed line) and II (solid lines); curves for model II correspond to different $\tau=10^4$; $1.5*10^3$; 750 from up to bottom; (*c*) dependence of model limiting $<R>$ values on τ (points) with corresponding power-law fit (solid line).

The proposed models are qualitatively compared **(Fig. 2a)** with respect to the time dependence of free monomer concentration, c_{mon}, whose experimentally found behaviour is proportional to the graph given in **Fig. 1**. As one can see, model I shows a significant increase in c_{mon} at a certain stage, which is in disagreement with the experiment. In contrast, for model II the time evolution of both free monomer concentration **(Fig. 2a)** and mean cluster size **(Fig. 2b)** has a monotonous character, which is close to the experimental one. This means that this model is a reasonable approach for describing cluster growth in fullerene polar solutions.

The change in the time dependence of mean cluster size, $<R>$, with varying τ is illustrated in Fig. 2b, where one can see that its limit is determined by τ. The found limits of $<R>$ in **Fig. 2b** are far from the real one, which means that significantly larger τ-values should be used in calculations. However, the corresponding numerical solution requires too much time resources, which are hardly available for the moment. The τ-value which fits experiment can be estimated from dependence $<R>$ vs. τ obtained at smaller cluster sizes **(Fig. 2c)**. It is of the power-law type, and the corresponding extrapolation for $<R>\sim100$ nm gives $\tau\sim10^8$ a.u.. Taking into account that initial supersaturation $c_{mon}(0)/c_{eq}$ can be higher, one can conclude that to fit the experimentally observed cluster size, the approximate τ estimate is within 10^6-10^8 a.u. for supersaturations of 10^4-10^6. Further work on the proposed models and their development is in progress.

References

[1] M. V. Avdeev, V. L. Aksenov, T. V. Tropin, Russ. J. Phys. Chem. A Vol. 84 No. 8, 1274 (2010).
[2] A. Mrzel, A. Mertelj, A. Omerzu, et al., J. Phys. Chem. **103**, 11256 (1999).
[3] V. L. Aksenov, M. V. Avdeev, T. V. Tropin, M. V. Korobov, N. V. Kozhemyakina, N. V. Avramenko, L. Rosta, Physica B **385**, 795 (2006).
[4] V. L. Aksenov, T. V. Tropin, M. V. Avdeev, V. B. Priezzhev, J. W. P. Schmelzer, Physics of Particles and Nuclei, **36**, S52 (2005).

SOLVATOCHROMISM IN FULLERENE SOLUTIONS

T.A.Kyrey[a,b], O.A.Kyzyma[a,b], M.V.Avdeev[a], V.L.Aksenov[a,c], M.V.Korobov[d], L.A.Bulavin[b]

[a]Joint Institute for Nuclear Research, Dubna, Moscow reg., Russia
[b]Kyiv Taras Shevchenko National University, Kyiv, Ukraine
[c]Russian Research Center Kurchatov Institute, Moscow, Russia
[d]Moscow State University, Moscow, Russia

Solutions of fullerene C_{60} in nitrogen-containing solvents (pyridine, N-methyl-2-pyrrolidone (NMP), benzonitrile and acetonitrile) and its mixtures are of current interest due to the time evolution of the electrooptical constant [1], as well as photoluminescence [2], IR [3], Raman [2] and UV-Vis spectra [4] which correlate with cluster formation.

In the given experiments we study solvatochromic effects after dissolution of C_{60}/NMP system. Previously, time-dependent solvatochromic effect (temporal solvatochromism) was observed in C_{60}/NMP solution [2]. Addition of polar solvent (water, miscible with NMP) to this system leads to sharp solvatochromic effect (at negligible changes of system's composition) and increasing of absorbance at 450-550 nm [5,6]. Here, the changes in UV-Vis spectra of fullerene C_{60} in mixture NMP/toluene at the solution polarity variation (ε = 3,8 ÷ 26,6) were investigated. Time-dependent study at increasing as well as decreasing of solvent polarity was done. Smearing of absorbance spectra for fullerene solutions in different polarity mixtures was observed. These solvatochromic effects are analyzed with respect to solvation processes.

Fullerenes (Fullerenovye Tekhnologii, purity > 99.5%) and solvents of different polarity: polar NMP (ε=32) (Merck, purity > 99.5%) and low-polar toluene (ε=2,4) (Merck, purity >99.5%) were used for samples preparation. The C_{60}/NMP solution was prepared by adding 20 mg fullerene in 34 ml NMP with stirring for one hour at room temperature The solution was stored in darkness at room temperature. To obtain the C_{60}/toluene solution the fullerene was dissolved in toluene and stirred for ten minutes. Ternary solutions C_{60}/NMP/toluene and C_{60}/toluene/NMP were obtained in two ways: by addition of toluene or NMP to initial C_{60}/NMP or C_{60}/toluene solution, respectively. The volume fraction of toluene or NMP in the final mixture was varied in the range of 20-95 % (ε = 3,8 ÷ 26,6). Absorption spectra were obtained using Hitachi U-2000 (wavelength range 200-1000 nm) UV-Vis spectrophotometer. Quartz cells with 2 mm path length were used. The spectra were obtained right after the solution preparation, several days after preparation and one month later.

The UV-Vis spectra of fresh C_{60}/NMP and C_{60}/toluene solutions are compared in fig.1. They both exhibit characteristic peaks of molecular C_{60} at about 330 and 410 nm with slight shifts, when comparing the two solutions, determined by a difference in the fullerene-solvent interaction. Changes in UV-Vis absorption spectra of C_{60}/toluene system at NMP addition are presented in Fig. 2. It is clearly seen that the addition of NMP to the C_{60}/toluene system leads to a smearing of specific peaks at λ = 330 nm and λ = 410 nm and also an increase in absorption at λ = 400 ÷ 550 nm.

The cluster formation [4] and fullerene salvation by NMP molecules take place after addition of polar components to solution (increase permittivity up to 26,6). New solvate C_{60}/NMP are formed and therefore absorbance spectra are changed. It should be noted that change of solution color from purple specific for the system C_{60}/toluene to yellow-brown specific for the system C_{60}/NMP and hypsochromic effect (the shift of the absorption peak towards higher energy) are observed (Fig. 3). There is indication about formation of donor-acceptor complexes between fullerene and solvent molecules [2].

Addition of toluene to C_{60}/NMP leads to decrease of solution polarity from 32 (C_{60}/NMP) to 3,8 (C_{60}/NMP/toluene with 95 vol. % of toluene). The sharp solvatochromic effect was observed when volume fraction of toluene in the ternary solution more than 80 vol. % (Fig. 4). In this case the spectrum of the system takes the form specific to the fullerene solution in toluene. It should be noted, that increase of low-polar component in the C_{60}/NMP/toluene solution leads to increase of selective salvation (considerable difference between composition of salvation shell and bulk solution) due to greater salvation power of NMP in compare to toluene. When volume fraction of toluene in solution up to 80% fullerene clusters are dissolve (transition from colloidal to molecular solutions) and UV-Vis spectrum takes form of molecular C_{60}/toluene solution.

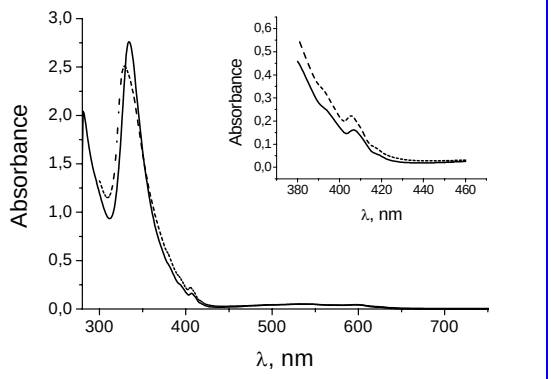

Fig. 1. UV-Vis spectra of fresh C_{60}/NMP (dash), and C_{60}/toluene (solid) solutions. Absorbance normalized to fullerene concentration. Inset shows peak shift at 410 nm

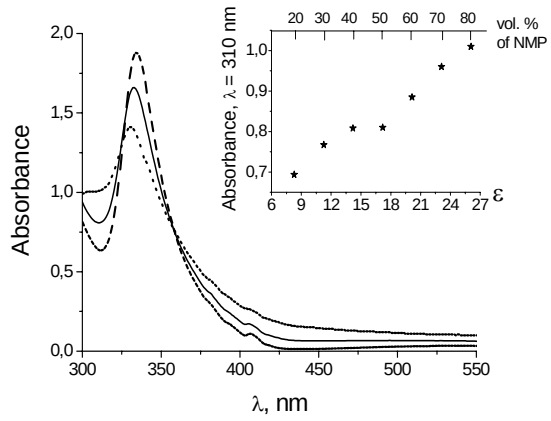

Fig. 2. UV-Vis spectra of C_{60}/toluene solution (dash) and C_{60}/toluene/NMP solutions at 50 vol. % (solid) and 80 vol. % (dot) of NMP. Inset: absorbance at wavelength of 310 nm versus dielectric constant (ε) and NMP vol. fraction (20-90%). Absorbance normalized to fullerene concentration

It should be noted that the addition of toluene to an old C_{60}/NMP system (with a smoothed spectrum) did not lead to any changes in the absorption spectra. In this case considerable amount of added toluene leads to partial cluster decomposition without complete transition to molecular solution. Similar effects were observed in C_{60}/NMP solution at water addition [7, 8].

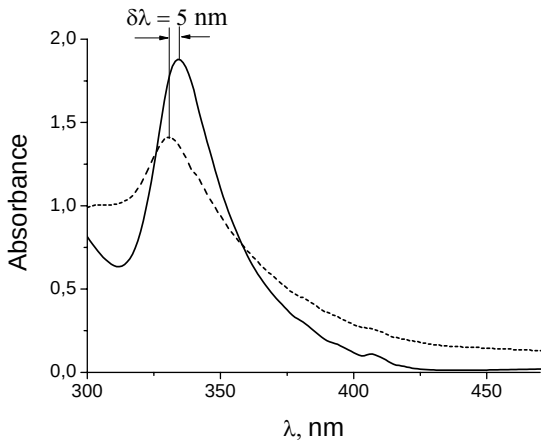

Fig. 3. Hypsochromic effect for C_{60}/toluene (solid) and C_{60}/toluene/NMP (dash – 80 vol. % of NMP) solutions. Absorbance normalized to fullerene concentration

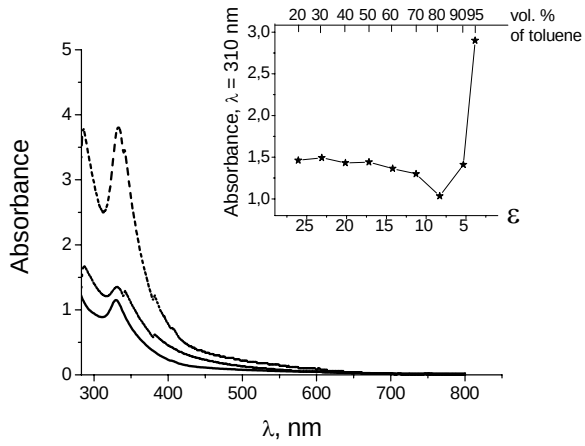

Fig. 4. UV-Vis spectra of C_{60}/NMP solution (solid) and C_{60}/NMP/toluene at 90 vol. % (dot) and 95 vol. % (dash) of toluene. Inset: absorbance at wavelength of 310 nm versus dielectric constant (ε) and toluene vol. fraction (20-95%). Absorbance normalized to fullerene concentration

It was shown [8], that C_{60}/NMP characterized by temporal solvatochromism (spectrum smearing with time). Similar temporal smearing (during one month) was observed for all samples of both systems (C_{60}/NMP/toluene and C_{60}/toluene/NMP) regardless the ratio NMP/toluene. The reason of temporal solvatochromism is formation of donor-acceptor complexes C_{60}/NMP due to high salvation power of NMP. Namely, selective salvation in ternary fullerene solutions with low NMP content takes place.

Sharp (change mixture composition) and temporal (with time) solvatochromism of fullerene solution in mixture N-methyl-2-pyrrolidone (NMP)/toluene at the solution polarity variation (ε = 3,8 ÷ 26,6) were observed. Addition of polar NMP to C_{60}/toluene solution leads to clusterization and formation of donor-acceptor complexes between C_{60} (acceptor) and NMP molecules (donor), which accompanied by hypsochromic effect and smearing of specific peaks at 330 and 410 nm. Decrease of fullerene solution polarity (toluene addition) leads to increase of selective salvation due to greater salvation power of NMP in compare to toluene. When volume fraction of toluene in solution up to 80% fullerene clusters in ternary solution are dissolve (transition from colloidal to molecular solution) and sharp solvatochromic effect are observed. In this case the spectrum of the system takes the form specific to the fullerene solution in toluene. The temporal solvatochromism occurred for all ternary fullerene solutions regardless the ratio NMP/toluene in mixtures. The reason of this effect is high salvation power of NMP, which leads to formation of donor-acceptor complexes C_{60}/NMP with time in all samples.

References

[1] Baltog I., Baibarac M., Mihut L., et al. // Romanian Rep. Physics. 57 (2005) 837.
[2] N.P. Yevlampieva, Yu.F. Biryulin, et al. // Coll. and Surf. A 209 (2002) 167.
[3] O.A. Kyzyma, M.V. Korobov, M.V. Avdeev et al. // Fullerenes, Nanotubes and Carbon Nanostructures.18 (2010) 458.
[4] Nath S., Pal H., Palit D.K., et al. // J. Phys. Chem. B. 102 (1998) 10158.
[5] Mrzel A., Mertelj A., Omerzu A., Copia M., Mihailovic D // J. Phys. Chem. B 103 (1999) 11256.
[6] Kyzyma O.A., Avdeev M.V., Aksenov V.L., Bulavin L.A., Snegir S.V. // FLNP Annual report 2007 123.
[7] L. Aksenov, M.V. Avdeev, T.V. Tropin, et al. // Physica B 385-386 (2006) 795.
[8] V.L. Aksenov, M.V. Avdeev, O.A. Kyzyma, L. Rosta, M.V. Korobov. // Cryst. Rep. 52 (2007) 479.

SANS STUDY OF WATER-BASED FERROFLUIDS FOR BRAIN CANCER THERAPY

M.V.Avdeev[a], A.V.Feoktystov[a,b], B.Mucha[c], V.M.Garamus[c], R.Willumeit[c], K.Lamszus[d], L.Vekas[e], O.Marinica[f], R.Turcu[g]

[a]*Frank Laboratory of Neutron Physics, Joint Institute for Nuclear Research, Dubna, Russia*
[b]*Kyiv Taras Shevchenko National University, Kyiv, Ukraine*
[c]*Helmholtz-Zentrum Geesthacht, Geesthacht, Germany*
[d]*University Medical Centre Hamburg Eppendorf, Hamburg, Germany*
[e]*Center for Fundamental and Advanced Technical Research, Romanian Academy, Timisoara Division, Timisoara, Romania*
[f]*University Politehnica Timisoara, Timisoara, Romania*
[g]*National Institute R&D of Isotopic & Molecular Technologies, Cluj-Napoca, Romania*

Applications of magnetic nanoparticles for biomedical purposes were actively developed in the last decade [1]. As an example, cancer treatment in what concerns controllable drug delivery [2], diagnostics (magnetic resonance imaging [3]), and therapy (magnetic hyperthermia [4]) can be mentioned. This raises the problem of synthesizing biocompatible ferrofluids or magnetic fluids (fine liquid suspensions of magnetic nanoparticles), which are stable and controllable in biological media under different conditions.

Recently, some progress in the synthesis of concentrated water-based magnetic fluids (φ_m >10%) has been achieved [5] for the double stabilization of nanomagnetite by saturated monocarboxylic acids with short carbon chains, such as lauric acid (LA, $C_{12}H_{24}O_2$) and myristic acid (MA, $C_{14}H_{28}O_2$). In the present experiments, we study the concentrated samples with one of the highest φ_m values among those for available water-based ferrofluids with long-term stability (at least 1 year). The key point is that a significant increase in the stabilized fraction of magnetite when using LA and MA indicates that there should be specific structural peculiarities in these fluids as compared to other stabilization schemes.

The measurements were made on the SANS-1 instrument [6] at the GKSS Research Centre. A differential cross section per sample volume (scattering intensity) that is isotropic over the momentum transfer vector q was obtained as a function of modulus $q=(4\pi/\lambda)\sin(\theta/2)$, where λ is the neutron wave length and θ is the scattering angle. Experiments were carried out in a standard way to cover a q interval of 0.06-2.5 nm^{-1}. The contrast variation was achieved by diluting the initial samples with different mixtures of light water (H_2O) and heavy water (D_2O) in a way, in which the D_2O content, η, in the final sample is varied from 0 to 90%.

The presence of aggregates in bulk ferrofluids is clearly observed in the SANS curves corresponding to different contents of D_2O in the carrier (Figure 1). The SLDs of the surfactants (about 0.10×10^{10} cm^{-2}) do not differ much from the SLD of water (-0.56×10^{10} cm^{-2}), which means that in pure H_2O the surfactant component in the fluid structures is almost matched and the scattering comes mainly from magnetite with an SLD of about 6.90×10^{10} cm^{-2}. The addition of D_2O with an SLD of 6.34×10^{10} cm^{-2} increases the contrast from surfactants against the carrier, so specific features appear in the scattering curves as compared to the H_2O case. We fail in fitting the experimental curves to the model of separate core-shell particles imitating spherical magnetite cores coated with a surfactant shell. Hence, the data in **Figure 1** are treated in terms of the approach of modified basic functions [7], which was recently applied well [8] to aqueous magnetic fluids with charge stabilization.

Resulting basic functions $I_c(q)$ for the two ferrofluids are given in **Figure 2**, together with their indirect Fourier transform (IFT) [9] in the form of the $p(r)$ function. Because shape scattering function $I_c(q)$ describes the effective homogeneous particles, the $p(r)$ function is the pair distance distribution (PDD) averaged over the particle shapes. The maximal values, where the $p(r)$ functions approach zero, correspond to the maximal aggregate sizes, which are 49 and 33 nm for samples LA+LA and MA+MA, respectively. The obtained values are in agreement with the dynamic light scattering data for similar samples [10] with reported average hydrodynamic sizes of 77 and 48 nm for fluids LA+LA and MA+MA, respectively. In particular, the average size ratios between the two fluids are similar:1.5 (SANS) and 1.6 (DLS). The radius of gyration, R_g, calculated from the $p(r)$ functions (15.2 ± 0.2 nm (LA) and 10.2 ± 0.1 nm (MA)) is connected to the radius of gyration of the particle shape, R_c, and volume, V_c, as $R_g^2 = \langle R_c^2 V_c^2 \rangle / \langle V_c^2 \rangle$, where the brackets denote the averaging over the particle radius distribution $D_n(R)$. Assuming the quasi-spherical shape of the aggregates, which allows one to use the relation $R_c^2 = (3/5)R^2$, one obtains the characteristic radii of the particles $(\langle R^2 V_c^2 \rangle / \langle V_c^2 \rangle)^{1/2}$ to be equal to 19.5 ± 0.3 and 13.8 ± 0.1 nm for fluids LA+LA and MA+MA, respectively. For comparison, the PDD functions calculated from the TEM data of separate particles are also given in **Figure 2b**.

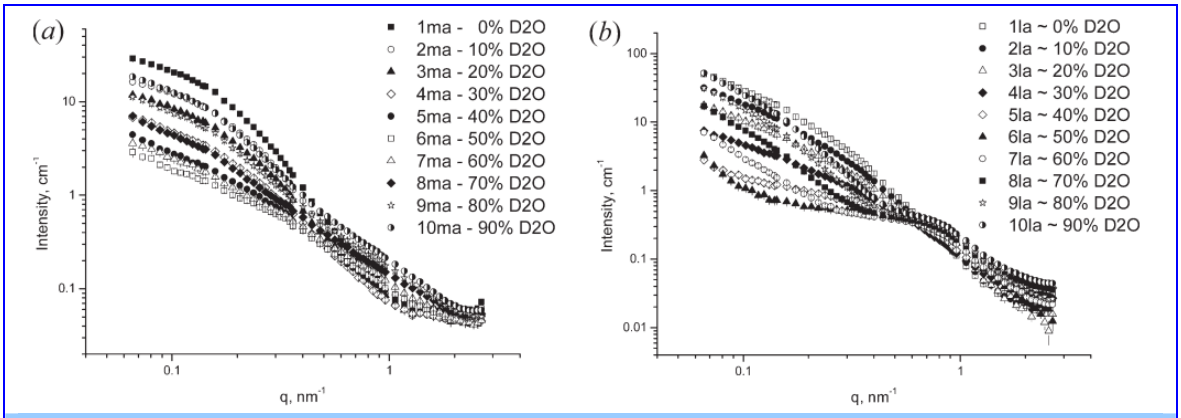

Fig. 1. SANS contrast variation for samples (a) MA+MA and (b) LA+LA. Sample labels correspond to the content of D_2O in the carrier.

Taking into account the mentioned difference in the $I_c(q)$ function and the scattering intensity in the case of pure H_2O (η =0), we compare the corresponding PDD functions in **Figure 2b**. It is interesting that such a difference is clearly seen only in the LA+LA sample. The maximal size from the $I_c(q)$ function is shifted up to about 7 nm from that of the magnetite component, which can be related well to the effective thickness (about 3.5 nm) of the surfactant shell around magnetite nanoparticles. The obtained thickness exceeds the doubled length of the LA molecule, 1.4 nm, which points to the bulky (nonoverlapped) structure of the stabilizing shell. In the MA+MA sample, both kinds of PDD functions are very similar, so the surfactant shell does not have any effect.

The incorporation of magnetite particles into cancer cells as a result of endocytosis were observed in optical microscope images of the samples stained with Berliner blue. The intensity of the absorbed magnetite correlates with the amount of ferrofluids initially added to the cancer medium. The toxicity rate depends on the cancer cell line. In some cases, the incorporation of magnetic particles slows the culture growth to 50-60%, but in other cases, such incorporation is almost nontoxic. At the same time, on average one can conclude that the magnetic particles that are used have some selective toxic effect with respect to the cancer cells. This follows from the fact that the cytotoxicity of the studied particles for astrocytes is low and does not depend on the initial particle concentration.

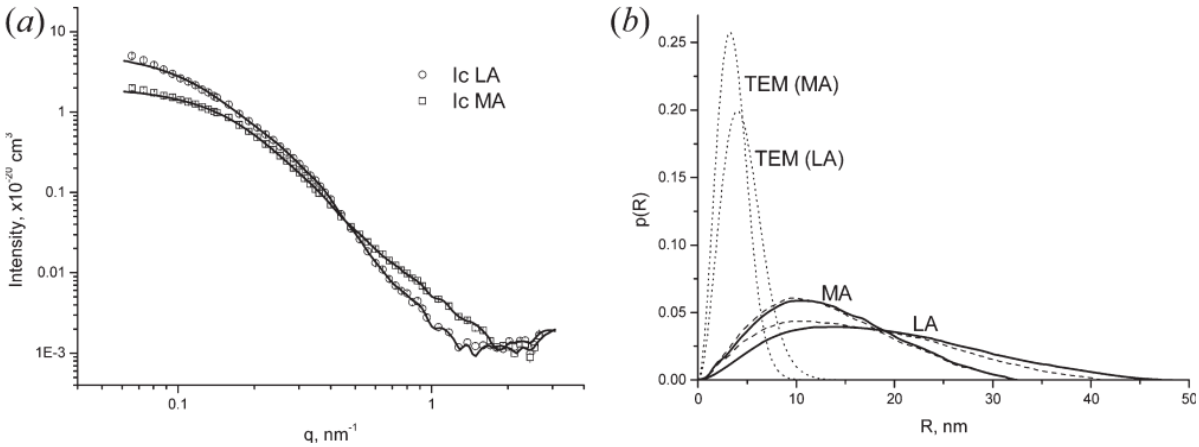

Fig. 2. (a) Experimentally obtained $I_c(q)$ basic functions for the two ferrofluids. The line shows IFT fits of the curves with parameters of R_g=15.1 ± 0.2 nm, $I(0) = (5.8 \pm 0.1) \times 10^{-20}$ cm^3 (LA+LA) and R_g = 10.7 ± 0.1 nm, $I(0) = (2.1 \pm 0.1) \times 10^{-20}$ cm^3 (MA+MA). (b) Pair distance distribution functions of particles found from $I_c(q)$ basic functions (−) are compared with the pair distance distribution functions from curves with 0% D_2O content (---) and from the TEM measurements of the individual particles (···).

So, the structure of water-based ferrofluids with double-layer sterical stabilization by short monocarboxylic acids (lauric and myristic acids) is described relative to their possible biomedical applications, in particular for cancer treatment. It is shown that besides discrete particles coated with a surfactant shell, a significant part of the particles are bound into aggregates. The inner structure of the aggregates differs for the two ferrofluids with respect to the relative content of

magnetite and surfactant, showing that in the case of myristic acid stabilization the magnetite particles are not fully coated with surfactant. Nevertheless, this factor does not have any significant effect on fluid stability in the absence of an external magnetic field. Both fluids can be used well in cancer (glioblastoma) treatment. As a source of magnetic nanoparticles, they show high stability in the cancer cell medium and provide a high incorporation of magnetic nanoparticles into cancer cells, which is strongly dependent on the cancer cell line. The magnetic particles from the probed ferrofluids are characterized by very low toxicity in human brain cells.

References

[1] Proceedings of the 7th International Conference on the Scientific and Clinical Applications of Magnetic Carriers, Vancouver, Canada, May21-24, 2008; Haeafeli, U., Zborowski, M., Eds.; J. Magn. Magn. Mater. 2009, Vol. 321.
[2] Berry, C.C.; Curtis, A.S.G. J. Phys. Appl. Phys. 2003, 36, R198–R206.
[3] Arbab, A.S.; Liu, W.; Frank, J.A. Expert Rev. Med. Dev. 2006, 3, 427–439.
[4] Brusentsov, N.A.; Nikitin, L.V.; Brusentsova, T.N.; Kuznetsov, A.A.; Bayburtskiy, F.S.; Shumakov, L.I.; Jurchenko, N.Y. J. Magn. Magn. Mater. 2002, 252, 378–380.
[5] Bica, D.; Vekas, L.; Avdeev, M.V.; Marinica, O.; Socoliuc, V.;Balasoiu, M.; Garamus, V.M. J. Magn. Magn. Mater. 2007, 311, 17–21.
[6] Zhao, J.; Meerwinck, W.; Niinkoski, T.; Rijllart, A.; Schmitt, M.; Willumeit, R.; Stuhrmann, H. Nucl. Instrum. Methods A 1995, 356, 133–137.
[7] Avdeev, M.V. J. Appl. Crystallogr. 2007, 40, 56–70.
[8] Avdeev, M.V.; Dubois, E.; Meriguet, G.; Wandersman, E.; Garamus, V.M.; Feoktystov, A.V.; Perzynski, R. J. Appl. Crystallogr. 2009, 42, 1009–1019.
[9] Pedersen, J.S. Adv. Colloid Interface Sci. 1997, 70, 171–210.
[10] Tombacz, E.; Bica, D.; Hajdu, A.; Illes, E.; Majzik, A.; Vekas, L. J. Phys. Cond. Mater. 2008, 20, 204103.

OBSERVATION OF NON-SPECULAR NEUTRON REFLECTION FROM A MAGNETIC FILM PLACED IN OSCILLATING MAGNETIC FIELD

S.V. Kozhevnikov[a], V.K. Ignatovich[a], Yu.V. Nikitenko[a], F. Radu[b], A. Rühm[c] and J. Major[c]

[a]Frank Laboratory of Neutron Physics, JINR, 141980 Dubna, Moscow Region, Russia
[b]Helmholtz-Zentrum Berlin für Materialien und Energie, Albert Einstein Strasse 15, D-12489 Berlin, Germany
[c]Max Planck Institut für Metallforschung, Heisenbergstr. 3, D-70569, Stuttgart, Germany

When the oscillating high frequency magnetic field is applied to the uniformly magnetized film, the neutron spin-flip takes place inside the film at the resonance condition. This leads to non-specular reflection in glancing geometry. We carried out an experiment to proof this phenomenon theoretically predicted in the articles [1-5].

The measurements were done at NReX$^+$ reflectometer (reactor FRM II, Garching, Germany). Fixed neutron wavelength 0.426 nm (1% FWHM) is used. The sample is the film of permalloy (500 nm) on the Si substrate. The sample sizes are 25×25×1 mm^3. The geometry of the experiment is shown in Fig. 1. The glancing angle of the incident beam is 0.4° and the angular divergence is 0.006°. The permanent magnetic field $H_0 = 20$ Oe is applied in the sample plane along the guide field. The oscillating magnetic filed with the amplitude $H_1 = 10$ Oe and the frequency about 30 MHz is applied in the sample plane along the beam path.

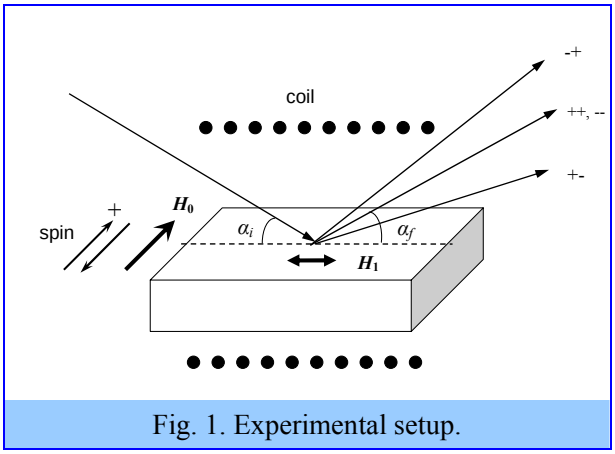

Fig. 1. Experimental setup.

At the resonant frequency non-specular reflection at 0.26° and 0.50° outgoing angles has been observed for both incident polarization up and down (Fig. 2).

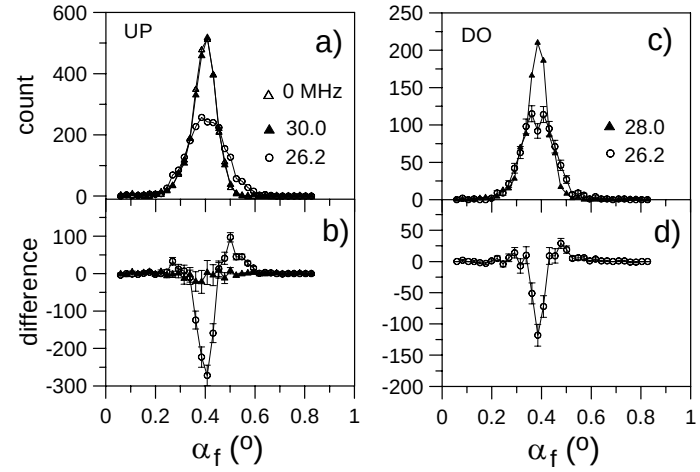

Fig. 2. Neutron count of reflected beam in dependence on outgoing angle.

Such big angular effect of beam-splitting corresponds to the energy changing in the internal magnetic induction 8.7 kG but not in the small external magnetic field 20 Oe. In Fig. 2 b one can see that there is no difference in reflected intensity in the cases of out-of-resonance frequency 30.0 MHz and switched-off frequency f=0 MHz.

In Fig. 3 the count of specularly reflected beam is shown in dependence on the frequency of the oscillating field (upper panels are integrated intensity, bottom panels are maximum of the intensity). One can see the resonance at 26.2 MHz (FWHM=1.2 MHz).

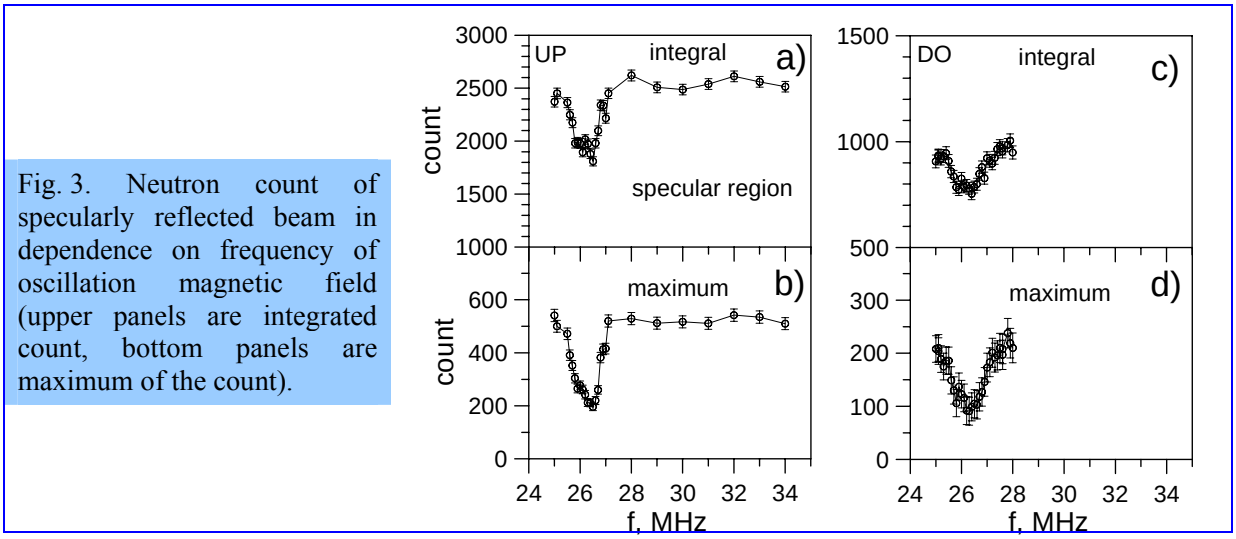

Fig. 3. Neutron count of specularly reflected beam in dependence on frequency of oscillation magnetic field (upper panels are integrated count, bottom panels are maximum of the count).

The effect of the specular intensity decreasing in the resonance consists of about 25 % for the integral and 50 % for the maximum. To define non-specular intensity effect we integrated intensity in two non-specular regions with frequency and extracted the intensity in the same regions with switched-off frequency for spin UP (see Fig. 4 a) or out-of-resonance frequency 28.0 MHz for spin DO (see Fig. 4 c). We define non-specular reflection probability (see Fig. 4 b,d) as the difference of non-specular intensity in Fig. 4 a normalized on out-of-resonance specular intensity integral in Fig. 3 (upper panels). The effect of non-specular intensity consists of 12% for the interval of $\alpha_f = 0.455° \div 0.641°$ and 3% for the outgoing angles $\alpha_f = 0.199° \div 0.338°$.

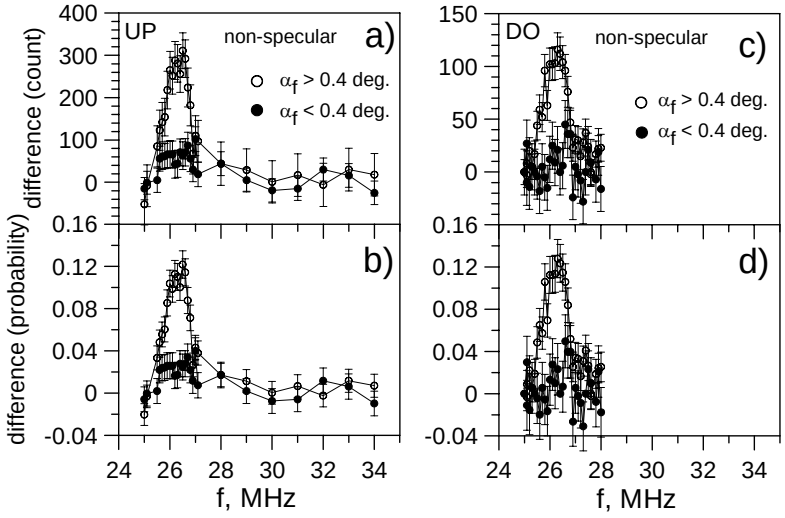

Fig. 4. Neutron count of non-specularly reflected beam in dependence on frequency of oscillation magnetic field. Upper panels are difference of count in- and out-of-resonance. Bottom panels are probability (difference of counts divided by the integrated intensity of the specularly reflected beam out-of-resonance).

In conclusion, we have observed experimentally non-specular neutron reflection from a uniformly magnetized film in an applied high-frequency oscillating magnetic field. The non-specular reflection takes place at resonance frequency. The resonance frequency corresponds to Larmor precession in the magnetic induction of the film. The value of angular beam-

splitting is big and cannot be explained by spin-flip in the external small magnetic field. For correct determination of the sign of spin-flip transitions, the following experiments with analyzer will be done.

The support of the management and staff at the FRM II, Garching, is gratefully acknowledged. This work was supported by a Focused Neutron Research Funding of the Max Planck Society, Munich. One of the authors (S.K.) is grateful to A.I. Frank for the interest to this subject and J. Franke for the technical help during the experiment.

References

[1] V.K. Ignatovich, F.V. Ignatovich, Am.J.Phys., 71 (2003) 1013.
[2] A.V. Kozlov, A.I. Frank, Physics of Atomic Nuclei, V.68, No.4 (2005) 1104-1119.
Yadernaya Fizika, V.68, No.4 (2005) 1149-1164.
[3] V.K. Ignatovich, Neutron optics, Moscow, Physmatlit, 2006, 335p.
[4] A.V. Kozlov, A.I. Frank, Physica B 404 (2009) 2550-2552.
[5] V.K. Ignatovich, Yu.V. Nikitenko, F. Radu, Nucl. Instr. and Meth. A 604 (2009) 653-661.

ULTRASONIC TREATMENT EFFECT ON THE LONG-TERM STABILITY OF BIOGENIC FERRIHYDRITE NANOPARTICLES SAMPLES IN AQUEOUS SOLUTION UNDER AMBIENT CONDITIONS

M. Balasoiu[a,b], L. Anghel[a,c], A. V. Rogachev[a], L.A. Ishchenko[d,e], A. Jigounov[f], G.M. Arzumanian[a], S.V. Stolyar[d,e], R.S. Iskhakov[d,e], Yu.L. Raikher[g]

[a]Joint Institute of Nuclear Research, Dubna, 141980, Russia
[b]Horia Hulubei National Institute of Physics and Nuclear Engineering, Bucharest, Romania
[c]Institute of Chemistry of ASM, Kisinau, Moldova
[d]Siberian Federal University, 660041, Krasnoyarsk, Russia
[e]Institute of Physics, Siberian Branch of RAS, 660036, Krasnoyarsk, Russia
[f]Institute of Macromolecular Chemistry, ASCzR Prague
[g]Institute of Continuum Media Mechanics, Ural Branch of RAS, 614013, Perm, Russia

Introduction

Ferrihydrite is an iron oxyhydroxide given the molecular formula $Fe_5HO_8 \cdot 4H_2O$, although $5Fe_2O_3 \cdot 9H_2O$ and others have been accepted. Ferrihydrite can show from two to six X-ray diffraction lines and nanoparticles are typically 2-10 nm in size. Structurally, ferrihydrite is believed to be based on simple chains of iron octahedral, although tetrahedrally coordinated iron has also been proposed. Ferrihydrite large surface area to volume ratio gives it high sorptive capabilities especially towards the heavy and transition metals, which are of environmental and industrial importance [1].

The literature [2] gives several methods for synthesis and purification of ferrihydrite. Although ferrihydrite occurs mainly in situations where Fe^{2+} is oxidized rapidly and/or where crystallization inhibitors are present. Oxidation can proceed via an inorganic pathway, but may also be assisted by micro-organisms.

In the present work methods to improve long-term stability of biogenic ferrihydrite nanoparticles produced by *Klebsiella oxytoca* are investigated. Earlier, it was shown that ferrihydrite nanoparticles produced by bacteria *Klebsiella oxytoca* in the course of biomineralization of iron salt solutions from natural medium [3] exhibit unique magnetic properties: they are characterized by both the antiferromagnetic order inherent to a bulk ferrihydrite and spontaneous magnetic moment due to the decompensation of spins in sublattices of nanoparticles [4]. Also, it was established that bacterium *Klebsiella oxytoca* creates two types of ferrihydrite nanoparticles as a result of variation of the growth conditions for the microorganisms, whose differences are accurately identified by means of Mossbauer spectroscopy [5, 6] static magnetic measurements analysis [6, 7] scanning electron microscopy and small angle X-ray scattering methods [8] on dry powder samples. The investigations in the direction of biomedical applications have revealed that the particles do not present cytotoxity and when attached to specific drugs present a weak antitumor activity against Ehrlich ascites carcinoma in mice [9].

Microstructure investigations of these biogenic nanoparticles by means of SAXS and SANS need special prepared samples: ferrihydrite nanoparticles dispersed in aqueous solution. Preliminary particle size analysis using high-resolution transmission electron microscopy images (HRTEM) combined with small angle X-ray scattering structure investigation of biogenic ferrihydrite aqueous suspensions are reported in [10]. Characteristic size of the particles (1-2 nm) (**Figure 1a**) estimated from HRTEM observations agrees with the height value of the objects identified by the small angle X- ray scattering data fit. Also the presence of organic material is detected by means of HRTEM. The nanoparticles or clusters of nanoparticles are withheld in the organic network (**Figure 1b**).

The low stability of the aqueous dispersions of the samples obtained from bacterial metabolism up to now made difficult detailed methodological SAXS and SANS studies.

Thus, effective methods to improve the stability of the biogenic ferrihydrite liquid dispersions are needed. Here results on the influence of ultrasonic treatment on the stability of before mentioned aqueous dispersions are reported.

Materials

Aqueous samples of biogenic particles of ferrihydrite were provided by Siberian Federal University, Krasnoyarsk, Russia. Ferrihydrite particles were obtained from microorganism isolated from Lake Borove (Krasnoyarsk krai). Initial concentration of magnetic nanoparticles in aqueous solution was 12.5g/l (5g of ferrihydrite powder dissolved in 400 ml double distilled water). From initial solution were prepared 4 samples of different concentration: $7.41 \cdot 10^{-3}$M, $5.54 \cdot 10^{-3}$M, $3.70 \cdot 10^{-3}$M, $1{,}85 \cdot 10^{-3}$M.

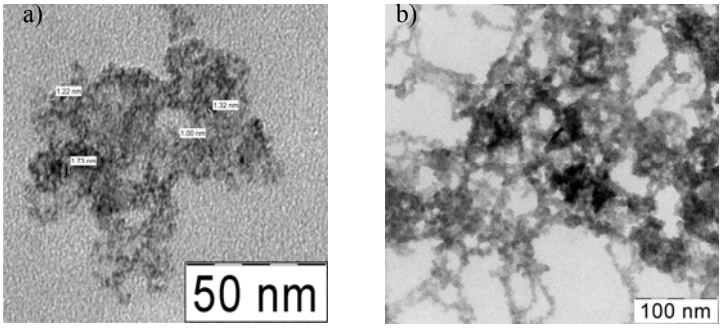

Fig. 1. HRTEM images of a sample of ferrihydrite nanoparticles dispersion in water: (a) and (b).

Prepared samples of different concentration of ferrihydrite were treated for two hours using a TRANSSONIC 310/H ultrasonic bath. Characterization of ultrasonic ferrihydrite samples in time consisted monitoring of visible spectra analysis on spectrophotometer. The absorbtion spectra of the samples with different ferrihydrite concentrations are presented in **Figure 2**.

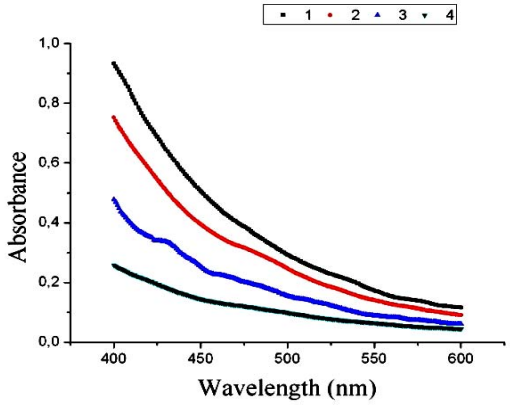

Fig. 2. Absorption spectrum vs concentration of ferrihydrite: (1) concentration of ferrihydrite $7.41 \cdot 10^{-3}$M; (2) concentration of ferrihydrite $5.54 \cdot 10^{-3}$M; (3) concentration of ferrihydrite $3.70 \cdot 10^{-3}$M; (4) concentration of ferrihydrite $1{,}85 \cdot 10^{-3}$M

Results and discussion

Due to its high sorptive properties, it is difficult to purify the biogenic ferrihydrite from organic matter and to maintain it dispersed in aqueous solution for a long time. We attempted the ultrasonic treatment as a physical method to disperse particle agglomerates without causing changes in chemical composition of the sample. The ferrihydrite concentration varied in each sample ultrasonic treated. A spectrum of ferrihydrite solution before ultrasonic treatment is shown in **Figure 2.1.** The spectrum is rather nondescript with gradual absorbance decline from 400 to 650 nm. For comparison purposes, the spectrum of the same ferrihydrite sample after ultrasonic treatment is shown in **Figure 2.2**.

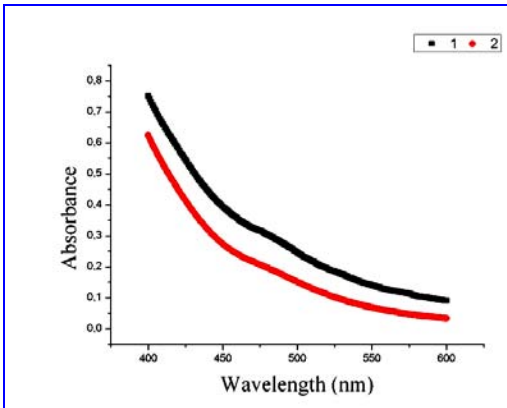

Fig. 3. Absorption spectrum of ferrihydrite sample of concentration $5.54 \cdot 10^{-3}$M: (1) before ultrasonic treatment; (2) after ultrasonic treatment

Visible spectra of ferrihydrite samples have shown changes after ultrasonic treatment. Decrease of absorbance values might be related to the reduction of the particles size. We also attempted to monitor the visible spectra of ultrasonic treated samples of ferrihydrite after 24h, 36h, 72h, and one week. The obtained data show that the samples remain stable during one week after ultrasonic treatment.

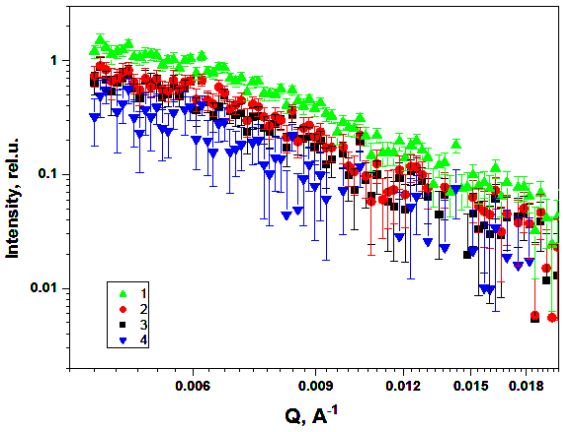

Fig. 4. SAXS experimental curves from biogenic ferrihydrite aqueous dispersions of following particle concentrations obtained at Rigaku spectrometer in function at IMC (Prague): (1) concentration of ferrihydrite $7.41 \cdot 10^{-3}$M; (2) concentration of ferrihydrite $5.54 \cdot 10^{-3}$M; (3) concentration of ferrihydrite $3.70 \cdot 10^{-3}$M; (4) concentration of ferrihydrite $1.85 \cdot 10^{-3}$M.

In **Figure 4** are presented SAXS experimental curves from biogenic ferrihydrite aqueous dispersions of four particle concentrations (after ultrasonic treatment) measured at Rigaku spectrometer in function at IMC (Prague): (1) $7.41 \cdot 10^{-3}$M; (2) $5.54 \cdot 10^{-3}$M; (3) $3.70 \cdot 10^{-3}$M; (4) $1{,}85 \cdot 10^{-3}$M. Further experimental data treatment is in progress.

References

1. Mabe D.R., Khasanov A.M., Stevens J.G., Hyperfine Interact (2005) 165: 209–213.
2. Schwertmann U., Cornell R.M., *Iron oxides in the laboratory. Preparation and characterization,* Wiley-VCH Publishing House Second Edition 2000, 8:103-113.
3. S. V. Stolyar, O. A. Bayukov, Yu. L. Gurevich, E. A. Denisova, R. S. Iskhakov, V. P. Ladygina, A. P. Puzyr', P. P. Pustoshilov, M. A. Bitekhtina, Inorganic Materials Vol.42, 763 (2006).
4. Yu. L. Raikher, V.I. Stepanov, S.V. Stolyar, V.P.Ladygina, D.A.Balaev, L.A. Ishchenko, M.Balasoiu, Phys. of Solid State, Vol.52, No.2, 277 (2010).
5. S.V. Stolyar, O.A. Bayukov, Yu.L. Gurevich, E.A. Denisova, R.S. Iskhakov, V.P. Ladygina, A.P. Puzyr', P. P. Pustoshilov, L.A. Cekanova M. A. Bitekhtina, Materialovedenie, No.7, 34 (2006) (Rus).
6. S. V. Stolyar, O. A. Bayukov, Yu. L. Gurevich, V. P. Ladygina, R. S. Iskhakov, P. P. Pustoshilov, Inorganic Materials Vol.43, 638 (2007).
7. Yu.L. Raikher and V.I. Stepanov, Journ. Exp. Theor. Phys., Vol.107, No.3, 435 (2008).
8. M. Balasoiu, S. V. Stolyar, R.S. Iskhakov, L.A. Ishchenko, Y.L. Raikher, A. I. Kuklin, O. L. Orelovich, Y. S. Kovalev, T. S. Kurkin, G.M. Arzumanian, Rom. Journ. Phys. Vol 55, No.7-8, 782 (2010).
9. L.A. Ishchenko, S.V. Stolyar , V. P. Ladygina, Y. L. Raikher, M. Balasoiu, O. A. Bayukov, R., S. Iskhakov, E. V. Inzhevatkin, International Conference on Magnetic Fluids ICMF12, 1-4 August 2010, Senday, Japan.
10. M. Balasoiu, L.A. Ischenko, S.V. Stolyar, R.S. Iskhakov, Yu.L. Raikher, A.I. Kuklin, D.V. Soloviov, T.S. Kurkin, D. Aranghel, G.M. Arzumanian, Optoelectronics and Advanced Materials –Rapid Communications, Vol. 4, No. 12, 2136 (2010).

STRUCTURAL AND MAGNETIC PHASE TRANSITIONS IN MULTIFERROIC $BiMnO_3$ AT HIGH PRESSURES

D.P.Kozlenko[a], A.A.Belik[b], S.E.Kichanov[a], D.V.Sheptyakov[c], Th.Straessle[c] and B.N.Savenko[a]

[a]Frank Laboratory of Neutron Physics, JINR, Dubna, Russia
[b]International Center for Materials Nanoarchitectonics, National Institute for Materials Science), Japan
[c]Laboratory for Neutron Scattering, ETH Zurich and Paul Scherrer Institut, Villigen, Switzerland

A great attention has been given to multiferroic effects, observed in $RMnO_3$ (R = Tb, Dy, Gd, Bi) compounds. In these materials ferroelectricity coexists with long range magnetically ordered ground state of incommensurate or commensurate nature. This leads to quite interesting novel physics, such as possibility of switching of electric polarization by magnetic field, very prospective for electronic devices, possible composite excitation of electromagnon, and promising many more surprises awaiting to be unearthed. The multiferroic $BiMnO_3$ is a rare example of the compound with collinear ferromagnetic ground state (T_{FM} = 100 K), possessing orbital order at T_{FE} = 500 K [1].

Our results [2] demonstrate that application of relatively moderate pressure ($P \sim 1$ GPa) leads to suppression of the initial FM ground state and appearance of the AFM ground state with the propagation vector k = (1/2 1/2 1/2) in $BiMnO_3$. The modification of the balance between FM and AFM superexchange interactions due to structural transformation is the possible reason for the observed magnetic phase transition. However, the structural details of high pressure phase of $BiMnO_3$, important for further elucidation of the nature of its multiferroic properties, remain unexplored.

The crystal structure of $BiMnO_3$ was investigated using the HRPT diffractometer [3] at the SINQ neutron spallation source (Paul Scherer Institute, Switzerland) at high pressures up to 10 GPa and ambient temperature. The incident neutron wavelength was 1.494 Å. The Paris-Edinburgh high pressure cell was used with a 4:1 volume mixture of fully deuterated methanol-ethanol as a pressure transmitting medium. For the pressure determination, an equation of state of NaCl, admixed to the sample in 1:2 volume proportions, was used.

The characteristic neutron diffraction patterns of $BiMnO_3$ measured at selected pressures up to 10 GPa and ambient temperature are shown in fig. 1. At ambient conditions the monoclinic structure of *C2/c* symmetry was detected. At pressures above 1 GPa, noticeable changes in diffraction data were observed, evidencing the structural phase transition. From the data analysis it was found that the structure of the high pressure phase of $BiMnO_3$ can be also described as monoclinic one with *C2/c* symmetry, but with different ratio of lattice parameters with respect to ambient pressure phase. The pressure-induced structural phase transition causes an increase of the *a* lattice parameter and decrease of *b* and *c* lattice parameters, while the unit cell volume decreases. The monoclinic angle β value is weakly affected.

At pressures above 8.5 GPa, appearance of another structural phase transition was observed in diffraction data (fig. 1). From the data treatment it was found that the crystal structure of the second high pressure phase has the *Pbnm* orthorhombic symmetry. Comparison between structural parameters of $BiMnO_3$ and those of related orthorhombic $RMnO_3$ compounds implies that a magnetic state modification from commensurate to incommensurate AFM one is expected at monoclinic-orthorhombic phase transition.

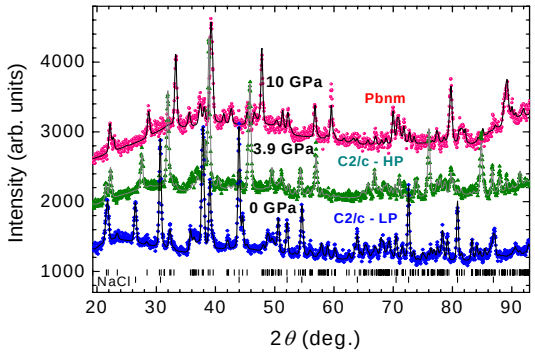

Fig. 1. Neutron diffraction patterns of $BiMnO_3$ measured at selected pressures and ambient temperature for two monoclinic (C2/c-LP and C2/c-HP) and orthorhombic structural phases and processed by the Rietveld method. Experimental points and calculated profiles are shown. Ticks below represent calculated positions of nuclear peaks of ambient pressure monoclinic phase (C2/c-LP) and NaCl, used for pressure calibration.

Our results demonstrate that suppression of the initial FM ground state and appearance of the AFM ground state accompanied by the structural phase transition between ambient pressure and high pressure monoclinic phases. The highly competing character of these magnetic interactions, resulting in a coexistence of FM and AFM phases under pressure, supports the mechanism of multiferroic phenomena in $BiMnO_3$ due to inversion symmetry breaking [2].

References

[1] T. Kimura, S. Kawamoto, I. Yamada, M. Azuma, M. Takano, and Y. Tokura, Phys. Rev. B 67, 180401(R) (2003).
[2] D. P. Kozlenko, A. A. Belik, S. E. Kichanov, I. Mirebeau, D. V. Sheptyakov, Th. Strässle, O. L. Makarova, A. V. Belushkin, B. N. Savenko, and E. Takayama-Muromachi, Phys. Rev. B 82, 014401 (2010).
[3] S.Klotz, Th.Strässle, G.Rousse, G. Hamel, and V. Pomjakushin, Appl. Phys. Lett. **86**, 031917 (2005).

A STUDY OF CLUSTER FORMATION IN SILICON GLASSES DOPED BY TiO_2/CeO_2 OXIDES.

S.E.Kichanov[a], S.A.Samoylenko[a,b], D.P.Kozlenko[a], A.V.Belushkin[a] L.A.Bulavin[b], G.P.Shevchenko[c], V.C.Gurin[c], V.Haramus[d] and B.N.Savenko[a]

[a]Frank Laboratory of Neutron Physics, JINR, Dubna, Russia
[b]Taras Shevchenko National University of Kiev, Kiev, Ukraine
[c]Research Institute for Physical Chemical Problems of the BSU, Minsk, Belarus
[d]GKSS, Geesthacht, Germany

The prospective material for optical filters is silicon glasses with doped oxides of the transition and rare earth elements [1]. Such glasses are characterized by high ultraviolet radiation protection and thermal stability, and they are suitable for numerous technological applications, including the development of novel modifications of laser glasses, light filters and the imitation of gem production [2].

The glasses doped by cerium and titanium oxides are yellow–orange and the optical absorption edge can be shifted significantly by varying the CeO2/TiO2 concentrations ratio [3]. It was assumed that the thermal stability of the yellow–orange color in silicon glasses is a result of the formation of complex clusters Ce–Ti–O [3].

In order to study the structural characteristics of silicon glasses containing CeO2 and TiO2 oxides with different concentration ratios, small-angle neutron scattering experiments were carried out with the spectrometer SANS-1 [4] on the research reactor FRG-1 (GKSS, Germany).

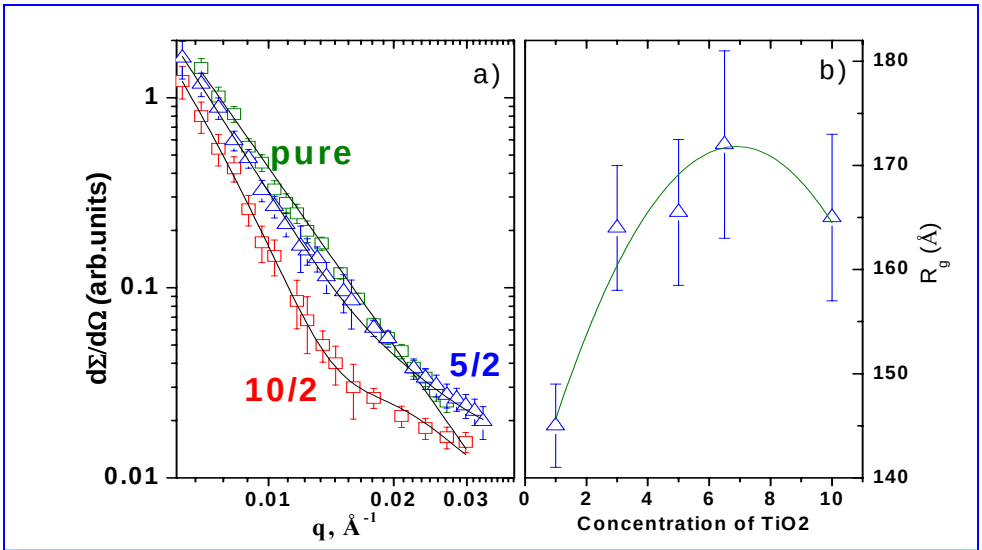

Fig 1. a) The small angle neutron scattering curves for pure silicon glass and glasses with a concentration ratio of TiO2/CeO2 oxides 5.0/2.0 and 10.0/2.0. The solid lines are calculated profiles. b) The calculated values of a gyration radius of the Ti-Ce-O clusters as function of TiO2 relative concentration (the concentration x (CeO2)=2.0). The solid line is polynomial fit.

The scattering curves for pure silicon glass and glasses with a molar concentration ratio of CeO2/TiO2 oxides 2.0/5.0 and 2.0/10.0 are shown in figure 1a. The curve for the pure glass indicates scattering from large objects - microscopic air bubbles, which appeared in the manufacture of glass material. The SANS curves of silicon oxides doped with CeO2/TiO2 exhibit somewhat different behavior. This corresponds to scattering from two different types of object, one related to larger air bubbles in the glass matrix and the other to smaller aggregates formed by Ce, Ti and O atoms. The experimental data were fitted by a function [5]:

$$d\Sigma(q)/d\Omega = Aq^{-\alpha} + C\exp(-\frac{1}{3}q^2R_g^2) + D$$

The calculated values of the gyration radius of those oxide clusters indicate weak nonlinear dependence of the cluster size on titanium oxide concentration (fig. 1b).

References

[1] G.S.Bogdanova, S.L.Antonova, and B.F.Dzhurinskii, Izv. Akad. Nauk SSSR, Neorg. Mater., 6, 943–948 (1970).
[2] W.Xu, S.Tang and W.Huang, "Fusion of glasses containing ceria and titania," J. Non-Cryst. Solids, 112, 186 – 189 (1989).
[3] E.E. Trusova, N.M. Bobkova, V.S. Gurin, and E.A. Tyavlovskaya, Glass and Ceramics Vol.66, Nos.7–8, 2009.
[4] H. B. Stuhrmann, N. Burkhardt, G. Dietrich, R. Jünemann, W. Meerwinck, M. Schmitt, J. Wadzack, R. Willumeit, J. Zhao, K. H. Nierhaus. Nucl. Instr. & Meth. A, **356** 133 (1995)]
[5] Brumberger H (ed) 1995 Modern Aspects of Small Angle Scattering (Dordrecht: Kluwer), p. 53.

MORPHOLOGY OF THE PHOSPHOLIPID TRANSPORT NANOSYSTEM

M.A. Kiselev[1], E.V. Ermakova[1], O.M. Ipatova[2], A.V. Zabelin[3]

[1] *Frank Laboratory of Neutron Physics, JINR, Dubna*
[2] *Institute of Biomedical Chemistry RAMS, Moscow*
[3] *Federal Scientific Center «Kurchatov Institute», Moscow*

Phospholipid transport nanosystem (FTNS) has different applications. First, FTNS is nanodrug with application at acute toxic exposure and at precomatose state. Second, FTNS is drug delivery system for 6 different antitumoral, antiphlogistic, and antioxidant drugs. Third, FTNS could be used as carrier for chlorin E6 in the photodynamic therapy and diagnostic. More important application of FTNS is drug delivery. A lot of studies have been carried out at the time of the design and medical test of FTNS. Nevertheless, the morphology of FTNS nanopartricle is not clear (vesicles or micelles?). Fig. 1 presents the vesicular morphology of FTNS with incorporated hydrophilic and hydrophobic drugs. Molecules of the hydrophobic (nonsoluble in water) drugs localized in the phospholipids bilayer. Molecules of the hydrophilic (water soluble) drugs locates inside of the vesicle.

The purpose of the presented experimental study was characterization of the FTNS morphology via small-angle X-ray scattering at the station DIKSI of synchrotron ring «Sibirea 2». Methodological purpose of the experiment was the development of the small-angle mode at the DIKSI beam line for the nanodiagnostic of nanodrugs. Data acquisition was carried out at sample to detector distance L_{sd}=30cm and 243.5cm, wavelength of the photons was λ=1.625Å. Samples were prepared as 25% and 50% dilution in water (w/w) of lyophilizated drug. At 25% of delution the sample consist of (w/w) 75% of water, 20% of maltose, and 5% of phospholipids as shown at Fig. 2. From the medical point of view, 25% concentration of drug corresponds to medical recipe for the intravenous injection. From physical point of view, 5% of phospholipids and 20% of maltose in water corresponds to the good X-ray contrast between maltose solution in water and phospholipids bilayer and not so strong intervesicle interaction [1-3]. It was shown in our previous study [1-3] that water solutions of disaccharides (sucrose, trehalose, maltose) create best experimental conditions for the characterization of phospholipid vesicular systems via X-ray small-angle scattering and allows to acquire the small-angle scattering curve in the broad q range.

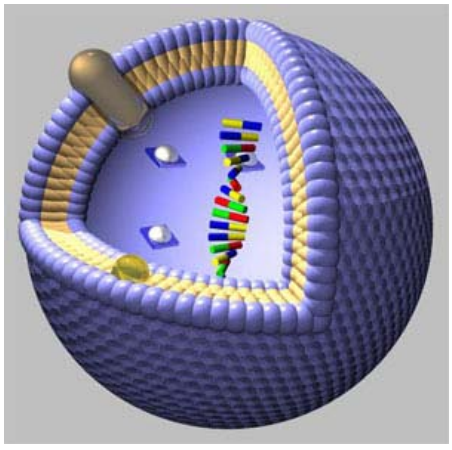

Fig. 1. Vesicular phospholipids based drug delivery system with incorporated hydrophilic and hydrophobic drugs.

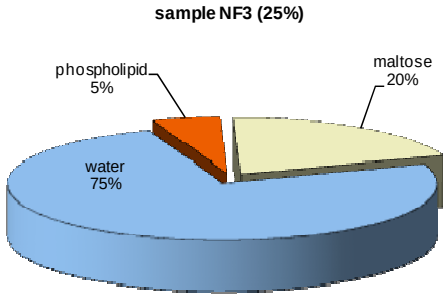

Fig. 2. Component distribution (w/w) in the sample under investigation (25% of FTNS).

The small-angle scattering curve from the sample 25% of FTNS is presented at Fig. 3. The small-angle scattering curve from extruded DMPC vesicles in 40% sucrose solution is presented for the comparison. This curve was obtained at beam-line D24 of synchrotron DCI, LURE, France. The line $1/q^2$ describes common law of scattering from the unilamellar vesicles with high value of polydispersity. Common direction of scattering curve from FTNS corresponds to the $1/q^2$, which is evidence of the vesicular morphology of FTNS nanoparticles after hydration. Comparison of scattering from extruded DMPC vesicles in 40% sucrose solution shows that FTNS vesicles in 20% maltose solution have low polydispersity. The polydispersity of FTNS vesicles is about 20-30%. The average vesicle radius 160Å for FTNS was calculated from the

position of first minimum in the form factor of the vesicle shape. DMPC vesicles after extrusion has larger radius - 210Å. FTNS consists from the unsaturated phospholipids – lecithin. Position of the first minimum in the form-factor of the bilayer at Fig. 3 shows that thickness of the bilayer from the lecithin is different from the thickness of fully saturated DMPC bilayer.

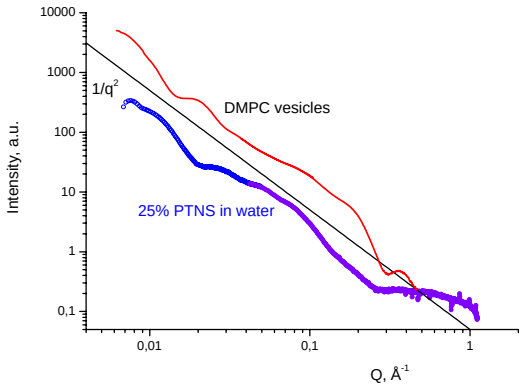

Fig. 3. Small-angle X-ray scattering curves: DMPC vesicles in 40% sucrose solution – red (LURE, France), 25% solution of phospholipid transport nanosystem (FTNS) in water – blue, law $1/q^2$ - black.

Presented result was first experiment at DIKSI beam line in the small-angle mode. Creation of the best experimental conditions for the investigation of lyophilizated nanodrugs has two contradictory requirements. Increasing of nanodrug concentration (low value of dilution in water) increase the interparticle interaction and create problem of artifact (form factor separation from the structure factor influence). Decreasing of nanodrug concentration decrease signal from phospholipids, but increase contrast from maltose. Comparison of experimental results from samples with different FTNS concentration shows that 25% FTNS in water (5% of lipid and 25% of maltose) create best experimental conditions for the investigation of lyophilizated nanodrugs in maltose without essential distortion and with good contrast.

Our previous study of disaccharides application for contrast variation in the SAXS experiment [1-3] allows one to start investigation the nanostructure of real drugs developed in the Institute of Biomedical Chemistry.

References

1. M.A. Kiselev, P. Lesieur, A.M. Kisselev, D. Lombardo, M. Killany, S. Lesieur, M. Ollivon. A sucrose solutions application to the study of model biological membranes. *Nuclr. Inst&Method A* 470 (2001) 409-416.
2. M.A. Kiselev, P. Lesieur, A.M. Kisselev, D. Lombardo, M. Killany, S. Lesieur. Sucrose solutions as prospective medium to study the vesicle structure: SAXS and SANS study. *J. Alloys and Compounds* 328 (2001) 71-76.
3. M.A. Kiselev, S. Wartewig, M. Janich, P. Lesieur, A.M. Kiselev, M. Ollivon, R. Neubert. Does sucrose influence the properties of DMPC vesicles? *Chemistry and Physics of Lipids* 123 (2003) 31-44.

МЕТОД СЛЕД-ОТОБРАЖЕНИЯ ДЛЯ РЕШЕТКИ ПЕЛЛА

Эльмар Аскеров

Лаборатория Нейтронографии им.Франка, ОИЯИ, Дубна, Российская Федерация
Институт Радиационных Проблем НАНА, Баку, Азербайджан

После экспериментального открытия квазикристаллов [1], эти новые объекты стали одной из перспективных направлений физики конденсированного состояния [2]. Существует большой интерес к одномерным квазикристаллам, так как имеется ряд нерешенных проблем в этой области, в числе которых и одна из существенных задач математики - классификация одномерных квазикристаллов.

Рассмотрим одномерную квазипериодическую решетку Пелла [3]. Одномерные квазикристаллы обычно описываются дискретным одномерным уравнением Шредингера, так как гамильтониан уравнения достаточно хорошо характеризует особенности квазипериодической структуры:

$$\sum\nolimits_j t_{ij}\psi_j = E\psi_i \ ,$$

где t_{ij} интегралы переноса, Ψ_j - волновая функция на *i*-ом узле.

Следуя [4] перепишем уравнение Шредингера в терминах трансфер-матриц. Нахождение волновых функций сводится к нахождению рекуррентной формулы для следа произведения матриц. Данный метод называют след-отображением.

В случае $t_{n,n+1} = t_{n,n-1} = 1$ мы получили рекуррентное соотношение для следа произведения матриц для решетки Пелла:

$$TrM_{n+1} = TrM_{n-1}\left(TrM_n\right)^2 - \frac{\left(TrM_n\right)^2 + TrM_{n-2}TrM_n}{TrM_{n-1}} - TrM_{n-1},$$

где M_n - так называемая трансфер-матрица для решетки длиной n. В этом случае данное след-отображение имеет интеграл движения (инвариант):

$$I = -xz + \left(\frac{x+z}{y}\right)^2 + y^2 \ , \text{ где}$$

$$x = TrM_{n+1}, y = TrM_n, z = TrM_{n-1} .$$

Полученная формула для следа произведения трансфер-матриц может быть использована для расчетов многих физических величин, таких как плотность уровней энергии, коэффициент трансмиссии и т.д.

Литература

[1] Shechtman D et al. Phys. Rev. Lett. 53 1951 (1984);
[2] Ю. Х. Векилов, М. А. Черников, УФН Т. 180 561—586 (2010);
[3] Gahramanov. I, Asgerov E., arXiv cond-mat.dis-nn:1010.24 (2010);
[4] M. Kohmoto, L. P. Kadanoff, and C. Tang, Phys. Rev. Lett. 50, 1870 (1983).

RESULTS OF MEASUREMENT THE RESIDUAL STRAINS IN THE WWER-1000 REACTOR VESSEL

V.V.Sumin[a], A.M.Balagurov[a] , I.V.Papushkin[a] , R. Wimpory[b]

[a] Frank Laboratory of Neutron Physics, Joint Institute for Nuclear Research, 141980, Dubna, Russia
[b] Helmholtz-Centrum Berlin for Material and Energy, D-14109, Berlin, Germany

Introduction

Owing to a high penetrability of thermal neutrons, neutron diffraction can be used to measure the distributions of residual stresses in a bulk of crystalline materials to depths of the order of several centimeters. The principle of the method is the measurement of the shift of the position of the diffraction peaks from the positions determined by the unit cell parameters of the undeformed material [1, 2]. Internal stresses existing in a material cause corresponding deformation of the crystal lattice, which, in turn, is manifested in the shift of the Bragg peaks in the diffraction pattern. This gives direct information on changes in the interplanar distances, from which the internal stresses can be easily calculated. At the present time, the method is widely used to determine residual stresses in bulk products and composites, to test welds, and to study complicatedly deformed products and behavior of materials during fatigue tests.

The strains due to internal stresses are usually of the order of 10^{-3}–10^{-4}; because of this, in order to measure such strains, a high resolution neutron diffractometer with $\Delta d/d = (3–5) \times 10^{-3}$ is used. In this case, the accuracy of determination of residual stresses in steels is 20–40 MPa. In this work, we studied the residual stresses in the natural WWER-1000 reactor vessel under stainless steel facing inside the vessel. The vessel base metal is the Grade 15KhGMFAA ferrite. The sign of the residual stresses in the direction parallel to the facing ferrite interface (tangential stress) is of great importance for the vessel corrosion resistance. As the tangential stresses are positive (tensile stresses), any crack in the stainless steel facing brings about cracking also in the ferrite. And vice versa, negative tangential stresses prevent the cracking.

Results

The view and scheme of measurements on the thick template are shown in **Fig. 1.** From the symmetry considerations, one can assume that the strains in both the tangential directions are equal, i.e., $\varepsilon_z = \varepsilon_y$. Because of this, we measured only one tangential component and also the normal component of the residual strains. The measurements were performed on a E3 stress diffractometer of the Hahn–Meitner Institute. The results of the measurements are presented in

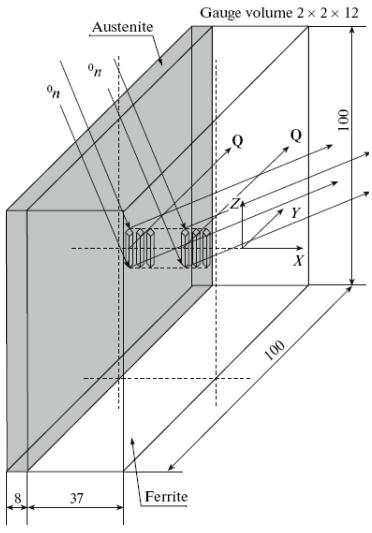

Fig. 1 Sizes and scheme of measurement of the tangential residual strains in the templet. Q is the scattering vector of neutrons.

Fig. 2. The measurements were performed in the normal direction from two sides of the specimen: on the side of the facing, to a depth of 5 mm in the ferrite phase and, on the side opposite to the facing, from the coordinate 34 to 17 mm inside the ferrite. We failed to measure the residual strains in the middle of the template because of the limitations in aperture ratio.

The residual stresses in the thick template were calculated by known relationships [1, 2] with the assumption $\varepsilon_z = \varepsilon_y$. As in the case of the thin template, the residual stresses under the facing in the ferrite phase remain negative, i.e., as aforementioned, favorable regarding the corrosion cracking, and they are somewhat lower (–140 MPa) in the thick template as compared to the thin template (–220 MPa). A reason of such a disagreement is the underestimate of the normal residual stresses ($\varepsilon x = 0$) for the thin template which are not really small: in the thick template, studied early on FSD-spectrometer the residual stresses are positive and are equal to 70 MPa .

The partial discrepancy between obtained neutron and cutting experimental results can be explained by the methodological differences of applied experimental techniques. But all methods showed qualitative consent.

Fig. 2. Residual stresses in studied template along phase interface. Vertical line indicates austenite-ferrite interface position at Z = 8 mm. Points represent residual stresses measured by neutron diffraction parallel to phase interface (♦ - σ_y, ■ - $\sigma_x \approx \sigma_z$). Dash curve represents stress kinetic intensity value obtained using crack propagation method while solid curve corresponds to the residual stress value estimated by cutting method.

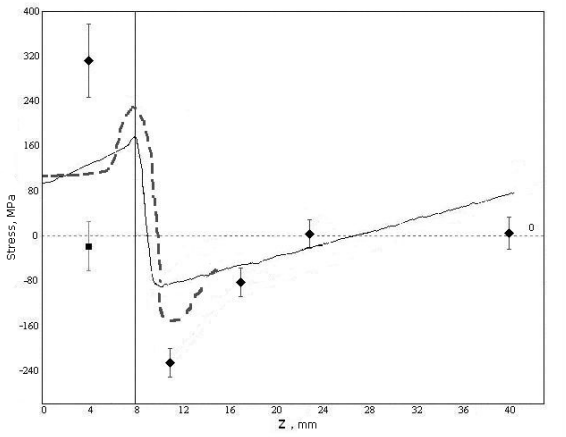

Acknowledgments

This study was supported by the International Scientific and Technical Centre (project no. 3074.2).

References

1. A. J. Allen, M. T. Hutchings, C. G. Windsor, and C. Andreani, Adv. Phys. **34**, 445 (1985).
2. V. L. Aksenov, A. M. Balagurov, G. D. Bokuchava, V. V. Zhuravlev, E. S. Kuz'min, A. P.Bulkin, V. A. Kudryashev, and V. A. Trunov, Soobshch. Ob'edin. Inst. Yad. Issled. P13_2001_30 (2001).

THE RESOLUTION FUNCTION OF A TOF REFLECTOMETER IN THE GRAVITY FIELD

I. Bodnarchuk[a], S.Manoshin[b], S.Yaradaikin[b], V.Kazimirov[b], and V.Bodnarchuk[b]

[a] Lomonosov Moscow State University, Skobeltsyn Institute of Nuclear Physics, Moscow, Russia
[b] Joint Institute for Nuclear Research, Frank Laboratory of Neutron Physics, Dubna, Russia

The effect of gravity on neutron scattering is negligible if a thermal spectrum up of to 10 Å is used. Modern cold sources produce spectra with an ample quantity of cold neutrons. Gravity may have a crucial role for the cold part of the spectrum in neutron scattering experiments demanding high angle resolution. It mainly concerns the reflectometry method where a small deviation in the angle distribution may lead to visible effects.

Presently, the new multifunctional time-of-flight (TOF) reflectometer, GRAINS, is under construction at the modernized high flux pulsed reactor with the new cold moderator, IBR-2M, in Dubna (Russia) [1]. It is necessary to study the influence of gravity on the resolution function because the principal feature of this reflectometer is the horizontal sample plane.

We consider the general configuration of elements, which defines the reflectometry mode including the source *M*, two slits *D1* and *D2*, sample *S* and a detector. The centers of the slits and the sample are on the line inclined at an angle $\theta = 15$ mrad to the horizontal plane. The angular resolution function for such reflectometer with parameters based on the real beam line characteristics of the reflectometer GRAINS was deduced by extending the analytical beam-analysis method [2], which took into account the influence of gravity. This function was obtained for the fixed neutron wavelength and then convoluted with the wavelength resolution function.

To test the approach, reflectivity curves smeared by the derived resolution function were compared with the reflectivity curves simulated by the VITESS Monte-Carlo software package [3]. A thin monolayer with a critical angle of 5.56×10^{-4} rad/Å and thickness of 1500 Å on a substrate with a critical angle of 4.17×10^{-4} rad/Å was used as an idealized sample. The wavelength dependence of reflectivity from such a monolayer consists of a sequence of narrow oscillations whose positions and shapes are very sensitive to the resolution factor. An incident spectrum of constant intensity for all wavelengths was used to exclude the factor of spectrum shape from consideration.

The dependence of the gravity effect on the distance between the second slit and the sample S_{D2S} and on the sample size L_S was analyzed. The reflectivities for two sample lengths, $L_S = 20$ mm and $L_S = 100$ mm, and three sample positions, $S_{D2S} = 0.033$ m or $S_{D2S} = 0.05$ m (the sample position right after the second slit for two sample lengths correspondingly), $S_{D2S} = 0.5$ m and $S_{D2S} = 1$ m are shown on Fig. 1.

It can be seen that the agreement between the theoretical calculations in the frame of proposed approach and the Monte-Carlo simulations by means of the VITESS package is very good. In all cases, the deviations of reflectivity with zero and non-zero gravity can be observed. An increase in the distance between the second slit and the sample leads to higher deviation. Two factors, both of which are due to the bending of neutron trajectories in the gravity field, contribute to the deviation. The first factor is the increase in the grazing incidence angle, which leads to the shift of reflectivity fringes to higher wavelengths. If the angular divergence increases, the fringes broaden, and the gravity shift becomes less distinguishable. The second factor is that neutrons fall before the sample, which leads to the flux deficiency for longer wavelengths. This effect is greater for a smaller sample length. In the case of non-zero gravity, each element of the reflectometer acts as a wavelength and angular filter while in the case of zero gravity, each element only selects angles.

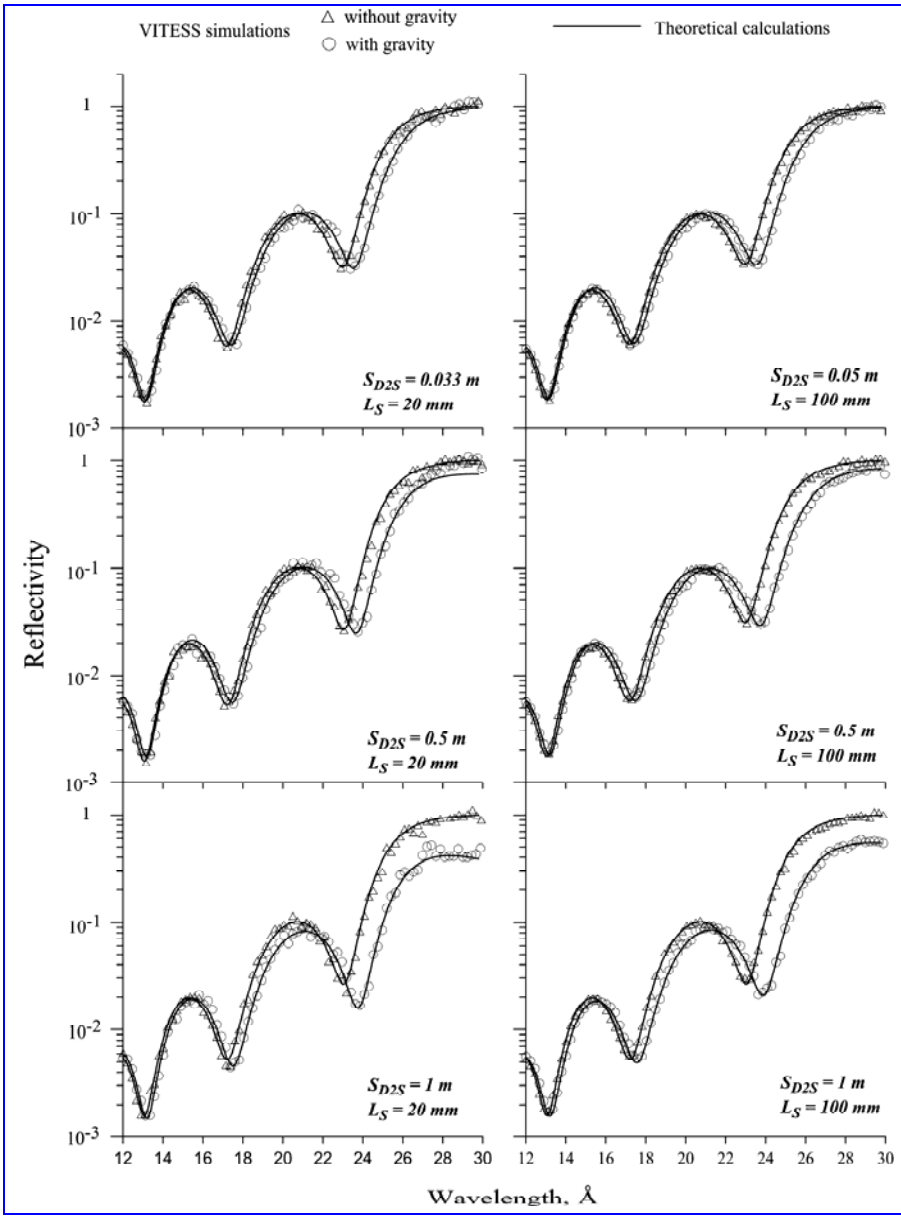

Fig. 1. The reflectivities for two sample lengths and three sample positions with respect to the second slit. The solid lines are the theoretical calculations, and the triangles and circles are the Monte-Carlo simulations prepared by the VITESS package with zero and non-zero gravity respectively. All plots are represented from 12 Å where all curves are distinguishable.

Conclusions

The analytical beam-line analysis method for deriving of the resolution function for the neutron TOF reflectometer accounting for effect of gravity was applied. The theoretical calculations are in good agreement with Monte-Carlo simulations, which mimic the real measurements with idealized samples. The proposed theoretical approach makes it possible to take the resolution into account correctly and allows one to carry out real measurements with a broad wavelength band.

References

[1] M.V. Avdeev, V.I. Bodnarchuk, et al., J. Phys.: Conf. Ser. 251 (2010) 012060;
[2] J.S. Pedersen, C. Riekel, J. Appl. Cryst. 24 (1991) 893;
[3] VITESS web site: <http://www.hmi.de/projects/ess/vitess>.

AQUEOUS SOLUTIONS OF POLY(ETHYLENE GLYCOL): SANS STUDY

G.Lancz[a], M.V.Avdeev[b], V.I.Petrenko[b,c], V.M.Garamus[d], M.Koneracká[a] and P.Kopčanský[a]

[a]Institute of Experimental Physics, Slovak Academy of Sciences, Košice, Slovakia
[b]Frank Laboratory of Neutron Physics, Joint Institute for Nuclear Research, Dubna, Moscow region, Russia
[c]Physics Department, Taras Shevchenko Kyiv National University, Kyiv, Ukraine
[d]GKSS Research Centre, Geesthacht, Germany

Hydrophilic poly(ethylene glycol) (PEG) is used for coating of colloidal particles for gaining biocompatibility. Its introduction into magnetic fluids (liquid dispersions of magnetic nanoparticles) may increase the circulation time of magnetic particles in organisms by hindering the action of the mononuclear phagocyte system (reticuloendothelial system), which is a part of the immune system. This is because nanoparticles, or surfaces in general, coated with PEG show enhanced resistance against protein adsorption, see e. g. [1] and references therein. An increase in biocompatibility of a given magnetic fluid is expected even by the simple addition of PEG, i.e. without a covalent bond between PEG and the magnetic particle. The goal of this study was to understand the structural characteristics of PEG molecules in water, which give some basic knowledge useful for further investigations of complex systems comprising PEG. In the given work the solutions of PEG in deuterated water (D_2O) with different molecular weights in a range of M_n = 400 – 20000 were investigated using small-angle neutron scattering (SANS) technique. Recently [2, 3], SANS was successfully applied for PEG in D_2O within a narrow range of M_n = 2000 – 8000 at different solution ion strength. Together with the compressibility and intermolecular distance as a function of PEG concentration [2], two possible structures (Gaussian coils and flat 'plates') of PEG were discussed [3] with respect to the scaling in the scattering as a function of M_n. Here, SANS characterization of PEG covers wider M_n-interval. Additionally, the measurements were performed at the physiological temperature of 37°C taking into account a specific interest for using PEG in biocompatible ferrofluids.

PEG with four different molar masses was purchased from Sigma-Aldrich ('average mol wt 400', 'typical M_n 1000', and '16000 - 24000') and Merck ('9000 - 11250 g/mol'). PEG with M_n = 400, 1000, 10000, 20000 was dissolved in pure D_2O (D-content 99.9%) with the mass fractions within an interval of 0.5–10%. D_2O was used to achieve a sufficient scattering contrast between PEG and the liquid carrier, as well as for reduction of the incoherent scattering background from hydrogen. SANS experiments were performed using the SANS-1 instrument located at the Neutron Facility at GKSS Research Centre, Geesthacht, Germany. Measurements were done at the temperature of 37 °C. For solutions of PEG with M_n = 400, the 5 mm thick quartz cells were used. In other cases the thickness of the cells was 2 mm. In all cases pure D_2O was used as a buffer (blank, background sample). To obtain the differential cross-section per sample volume (hereafter referred to as scattered intensity) in the absolute scale (cm^{-1}) the standard calibration [4] using the scattering from 1-mm water sample was made after the background, buffer (D_2O) and empty cell corrections.

Changes in the experimental SANS intensities are followed in **Fig.1** (examples are given for PEG 1000 and PEG 10000). One can see that at the PEG concentrations of less than 3% the scattering shows a pronounced Guinier-type behaviour corresponding to a form-factor of the polymer coils. At higher concentrations the correlations between coils results in the structure-factor effect at small q-values, which is rather different for masses below 1000 and above 10000.

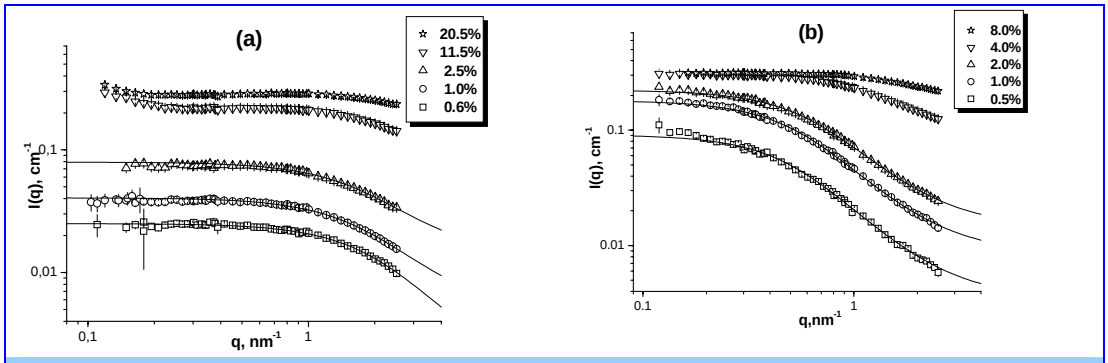

Fig. 1. Changes in SANS intensity (dots) with variation in mass fraction of PEG dissolved in D_2O, M_n is 1000 (a) and 10000 (b). Solid lines show fits in accordance with Debye formula (1) for non-interacting Gaussian coils.

Our interest in this study was the analysis of the coil form-factor. For this purpose the scattering data from low-concentrated (< 3%) solutions were first approached by the Guinier law to reveal the radius of gyration of the coil, R_g, at sufficiently small q-values ($qR_g \leq 1$). For low M_n (400 and 1000) the Guinier approximation is valid over the whole q-range covered in the experiments. This made possible to fit additionally the residual incoherent background caused by non-compensated hydrogen in PEG.

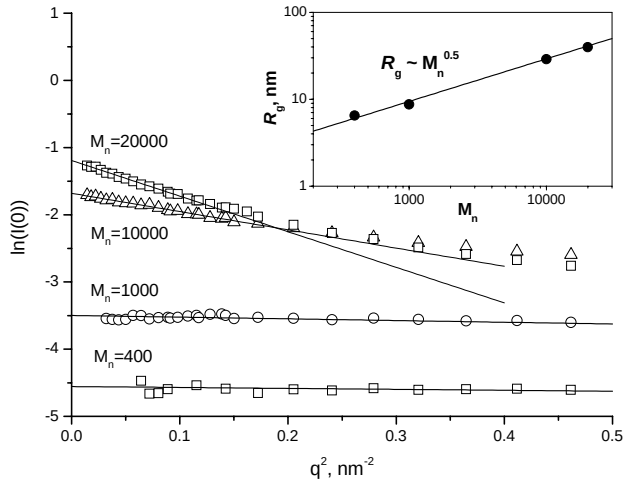

Fig. 2. Guinier plots of SANS intensity (dots) for 1% PEG solutions in D_2O with different M_n and corresponding linier approximations (lines) to regions $qR_g < 1$. Non-compensated incoherent background is subtracted. Several points with very low statistics in beginning parts of plots for M_n = 400 and 1000 are removed from treatment. Inset shows dependence of obtained radius of gyration on polymer molecular weight. Experimental errors do not exceed the size of dots.

It is important that this background was consistent for solutions with the same PEG concentrations independently of M_n. The Guinier approximations for 1% solutions of PEG with different masses are shown in **Fig.2**. The dependence of the obtained radius of gyration on the PEG molecular mass in this case (inset to Fig. 2) reveals a power-law behaviour (line in the double logarithmic scale) with an exponent of 0.48±0.02. This corresponds well to Gaussian coils (exponent 1/2) and coincides with the result for PEG with M_n= 2000 - 8000 in ionic solutions [3]. Hence, the Debye formula for the scattering from non-interacting Gaussian coils can be used at low PEG concentrations for any M_n. This is demonstrated in **Fig. 1**, where for diluted PEG solutions the fits are based on the formula:

$$I(q) = 2I_0[e^{-x} - (1-x)]/x^2 + B, \quad x = (qR_g)^2. \qquad (1)$$

Here, $I_0 = I(q \to 0)$ is the forward scattering intensity and B is the residual background. The same fit quality takes place for similar solutions with M_n of 400 and 20000. It should be noted that the relative difference in the values of the radius of gyration from the fit of the Debye formula (eq. 1) and from the Guinier appoximation is below 5%, and the Guinier approximation almost coincides with (1) in the overlapping region ($qR_g < 1$). Additionally, dependence of $q^2 \cdot I(q)$ vs. q reveals a typical behaviour for Gaussian polymer chains (not shown).

The observed scaling law $R_g \sim M_n^{0.5}$ in a wide polymer mass interval (400 – 20000) strongly confirms the Gaussian coil structure of PEG in water solutions. The scattering form-factor of the coils is well described by the Debye formula over the whole measured q-interval at the PEG concentration below 2 %. High adsorption properties of PEG for various substrates [5-7] and nanoparticles [8] also suggest a developed structure of this polymer.

References

[1] Y. Zhang, N. Kohler, M. Zhang, *Biomaterials* **23**, 1553 (2002).
[2] K.A. Rubinson, J. Hubbard, *Polymer* **50**, 2618 (2009).
[3] K.A. Rubinson, S. Krueger, *Polymer* **50**, 4852 (2009).
[4] G.D. Wignall, F.S. Bates, *J. Appl. Cryst.* **20**, 28 (1987).
[5] E. Tronel-Peyroz, H. Raous, D. Schuhmann, *J. Coll. Interface Sci.* **92**, 136 (1983).
[6] A.M. Mota, M.L. Simões Gonçalves, J.P. Farinha, J. Buffle, *Coll. Surf. A* **90**, 271 (1994).
[7] J.C. Dijt, M.A. Cohen Stuart, J.E. Hofman, G.J. Fleer, *Coll. Surf.* **51**, 141 (1990).
[8] M.V. Avdeev, A.V. Feoktystov, P. Kopčanský, G. Lancz, V.M. Garamus, R. Willumeit, M. Timko, M. Koneracká, V. Závišová, N. Tomašovičová, A. Juríková, K. Csach, L.A. Bulavin, *J. Appl. Cryst.* **43**, 959 (2010).

CONTRAST VARIATION IN SMALL-ANGLE NEUTRON SCATTERING ON WATER-BASED MAGNETIC FLUID WITH SODIUM OLEATE AND POLYETHYLENE GLYCOL STABILIZATION

M.V.Avdeev[a], A.V.Feoktystov[a,b], P.Kopcansky[c], G.Lancz[c], M.Timko[c], M.Koneracka[c], V.Zavisova[c], N.Tomasovicova[c], A.Jurikova[c], K.Csach[c], V.M.Garamus[d], R.Willumeit[d], L.A.Bulavin[b]

[a]*Frank Laboratory of Neutron Physics, Joint Institute for Nuclear Research, Dubna, Russia*
[b]*Taras Shevchenko Kyiv National University, Physics Department, Kyiv, Ukraine*
[c]*Institute of Experimental Physics, Slovak Academy of Sciences, Kosice, Slovak Republic*
[d]*Helmholtz-Zentrum Geesthacht, Geesthacht, Germany*

The structure description of complex (particularly polydisperse and multicomponent) systems is an important problem in modern nanoscience. Ferrofluids or magnetic fluids (fine stable dispersions of magnetic nanoparticles in liquids) belong to such a class of nanosystems. To ensure the long-term stability of ferrofluids in both unmagnetized and magnetized states, the magnetic nanoparticles are coated with a chemical layer, which prevents particle coagulation by attractive van derWaals and magnetic interactions. In biocompatible colloidal systems for medical applications, the chemical composition of the particle surface is of particular importance to avoid the action of the reticuloendothelial system, which is part of the immune system, in order to increase the lifetime of the magnetic nanoparticles in the blood stream. If magnetic particles in ferrofluids are coated with neutral and hydrophilic compounds such as polyethylene glycol (PEG) [1-3], the lifetime increases from minutes to hours or even days.

In present work, we investigate the above-mentioned water-based ferrofluid stabilized by sodium oleate, which is then modified by introducing biocompatible PEG. Several types of aggregates revealed in both ferrofluids complicate their reliable structure analysis. In this connection, we focus our investigation on the application of small-angle neutron scattering (SANS), which is one of the most suitable methods for studying the inner structure of colloidal particles in complex aggregate-containing systems. In particular, the contrast-variation technique (with H_2O/D_2O mixtures in the solvent) is used to reveal the scattering length density (SLD) distribution in various aggregates of non-magnetized samples at the scale of 1–100 nm.

The preparation of the ferrofluids studied here was based on a co-precipitation method that involved mixing two solutions ($FeSO_4 \cdot 7H_2O$ and $FeCl_3 \cdot 6H_2O$) with an alkaline aqueous medium (25% NH_3). The stabilization of the magnetite precipitate was achieved by the addition of sodium oleate ($C_{17}H_{33}COONa$, theoretical ratio 0.73 g to 1 g of Fe_3O_4). The system at this stage is discussed below as an initial ferrofluid and referred to as Sample 1. As a second stabilizer, PEG (M_w = 1000 g mol^{-1}) was added to the system (2.5 g per 1 g of Fe_3O_4). The experiments were carried out on the SANS-1 small-angle instrument at the FRG-1 steady-state reactor of the Helmholtz-Zentrum Geesthacht, Geesthacht, Germany (former GKSS Research Centre) [4]. No external magnetic field was applied to the samples.

The experimental data were treated in terms of the approach of [5] which, in addition to the classical contrast-variation technique [6], takes into account the polydispersity and magnetic scattering.

The experimental SANS curves for the two samples with different η are presented in **Fig.1**. The changes in the character of the curves are similar in both cases. Fluids with a low D_2O content (below 30%) show mainly the signal from magnetite. For higher D_2O content the contribution from the H-containing components becomes significant, which explains particularly the appearance of a broad peak (band) in the curves around $q \sim 0.8$ nm^{-1}. At the same time, some specific differences can be emphasized. First, the scattering from Sample 1 is significantly larger on the absolute scale. It resembles scattering from well defined particles, which is reflected in the existence of the Guinier regime at low q values.

In Sample 2, a degree of aggregation affects the curves, comparable to what is observed in water-based ferrofluids with double steric stabilization [7-10]. This is concluded from the power-law behavior of the scattering at low q values, which points to the fractal-type organization of the aggregates discussed below. The Guinier regime is not observed in the initial parts of the curves for these aggregates, which means that the aggregate size is beyond the instrument limit $D \sim 120$ nm (the estimate is derived from the minimum measured q value in accordance with the rule $D \sim 2\pi/q$).

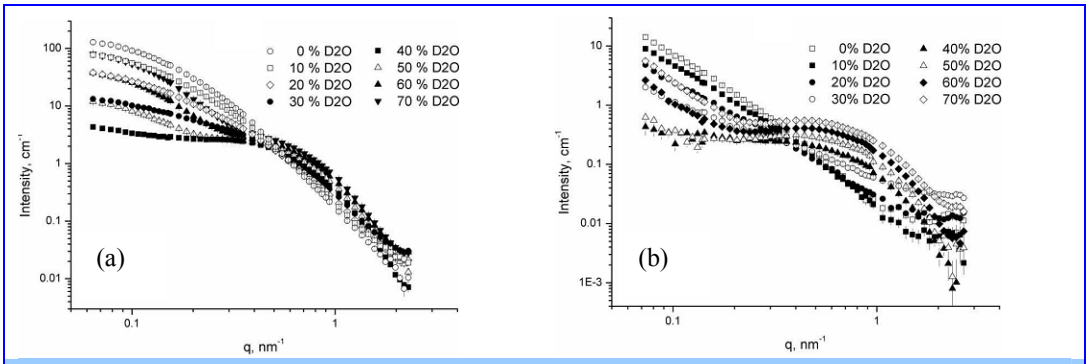

Fig. 1. Changes in the SANS curves with contrast variation for (*a*) Sample 1and (*b*) Sample 2. The percent volume fraction of D_2O in the solvent is indicated.

From the whole set of scattering curves the modified basic functions were calculated. The basic function $I_c(q)$ (Fig.2*a*) reflecting the average shape scattering differs greatly for the two samples in the initial parts of the curve (q <0.4 nm^{-1}).

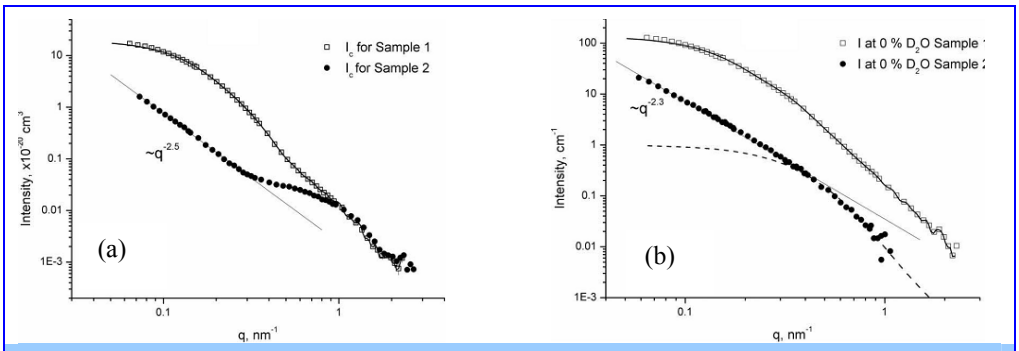

Fig. 2. (*a*) Experimentally obtained $I_c(q)$ basic functions (shape scattering) for Samples 1 and 2, compared with (b) the curves at 0% D_2O (scattering from magnetite only). Solid lines for Sample 1 correspond to IFT fits. Solid lines for Sample 2 show power-type scattering with the indicated exponents. The dashed line for the curve at 0% D_2O in (*b*) shows the scattering from separate magnetite nanoparticles (R_0 = 3.4 nm, S = 0.38).

It may be concluded that there is a transition from well defined particles in the case of Sample 1 to smaller particles and large aggregates in Sample 2. The new aggregates can be associated with fractal structures, which determine scattering of a power-law type with an exponent of about −2.5. This corresponds to a mass fractal dimension D =2.5 [11]. The behavior of the curves at high q values is similar and they show certain types of bands. For comparison, in **Fig.2*b*** the scattering curve obtained at η = 0 (light water) is given. At low q values, the character of the curves repeats those of the $I_c(q)$ functions, thus proving that magnetite particles mainly determine the shape scattering. At high q values, the curves differ significantly from the $I_c(q)$ functions. In particular, the bands disappear, which means that their origin is connected with particles composed of H-containing components.

We relate the bands above q ~ 0.3 nm^{-1} in the $I_c(q)$ functions to micelles of free sodium oleate in the solvent. At the highest q values the two functions differ by only a factor showing that the micelle concentration is about 30% higher in Sample 2 than in Sample 1. Additionally, the contribution from the micelles is more significant in the case of Sample 2, when the scattering from the magnetite particles decreases. In this case, the Guinier region for the micelles is well resolved. It was treated by indirect Fourier transform (IFT), taking into account the power-law scattering at low q values. If a spherical shape is assumed for the micelles, the resulting radius of gyration of the micelles, R_{gmic} = 1.59(5) nm, gives R = 2.05 nm according to the well known equation $R^2_{gmic} = (3/5)R^2$. The obtained value correlates well with the molecular length of sodium oleate.

So, the structures of a water-based ferrofluid with magnetite stabilized by sodium oleate and its mixture with PEG have been revealed by the contrast-variation technique in small-angle neutron scattering experiments. In particular, the addition of PEG leads to reorganization of the aggregate structure compared with the initial ferrofluid. Notably, a type of

exchange of packed and comparatively small aggregates (about 40 nm) with developed and large aggregates (above 120 nm) is observed, which is caused by the adsorption of PEG on the magnetite particles. Aggregates in both kinds of ferrofluids are stable with respect to time and temperature increase (343K).

References

[1] Timko, M., Koneracka ,M., Kopcansky ,P., Tomori, Z., Vekas, L., Jozefczak, A., Skumiel, A., Radenovic, A., Dietler, G., Bystrenova, E. & Lita, M. (2004). Indian J. Eng. Mater. Sci. 11, 276–282.

[2] Tomasovicova ,N., Koneracka ,M., Kopcansky ,P., Timko, M. & Zavisova ,V. (2006). Meas. Sci. Rev. 6, 32–35.

[3] Hong, R.Y., Ren, Z.Q., Han, Y.P., Li, H.Z., Zheng, Y. & Ding, J. (2007). Chem. Eng. Sci. 62, 5912–5924.

[4] Zhao, J., Meerwinck, W., Niinkoski, T., Rijillart, A., Schmitt, M., Willumeit, R. & Stuhrmann, H.B. (1995). Nucl. Instrum. Methods Phys. Res. Sect. A, 356, 133–137.

[5] Avdeev, M.V. (2007). J. Appl. Cryst. 40, 56–70.

[6] Stuhrmann, H.B. (1995). Modern Aspects of Small-Angle Scattering, edited by H. Brumberger, pp.221–253. Dordrecht: Kluwer Academic Publishers.

[7] Balasoiu, M., Avdeev, M.V., Aksenov, V.L., Hasegan, D., Garamus, V.M., Schreyer, A., Bica, D. & Vekas, L. (2006). J. Magn. Magn. Mater. 300, e225–e228.

[8] Wiedenmann, A., Hoell, A. & Kammel, M. (2002). J. Magn. Magn. Mater. 252, 83–85.

[9] Avdeev, M.V., Aksenov, V.L., Balasoiu, M., Garamus, V.M., Schreyer, A., Torok, Gy., Rosta, L., Bica, D. & Vekas, L. (2006). J. Colloid Interface Sci. 295, 100–107.

[10] Feoktystov, A.V., Bulavin, L.A., Avdeev, M.V., Vekas, L., Garamus, V.M. & Willumeit, R. (2009). Ukr. J. Phys. 54, 266–273.

[11] Schmidt, P.W. (1995). Modern Aspects of Small-Angle Scattering, edited by H. Brumberger, pp.1–56. Dordrecht: Kluwer Academic Publishers.

СОЗДАНИЕ МАКЕТА ТЕХНОЛОГИЧЕСКОЙ СИСТЕМЫ КРИОГЕННОГО ЗАМЕДЛИТЕЛЯ С ЭЛЕКТРОНИКОЙ УПРАВЛЕНИЯ И КОНТРОЛЯ

Ананьев В.Д., Беляков А.А., Богдзель А.А., Булавин М.В., Верхоглядов А.Е., Кулагин Е.Н., Куликов С.А., Кустов А.А., Мухин К.А., Петухова Т.Б., Сиротин А.П., Федоров А.Н., Шабалин Е.П., Шабалин Д.Е., Широков В.К.

ЛНФ, ОИЯИ

Введение

Криогенный замедлитель на основе ароматических углеводородов на мощном импульсном исследовательском реакторе ИБР-2 (КЗ) - будет уникальным импульсным источником холодных нейтронов с длиной волны более 0.3 нм, обеспечивающим проведение на современном мировом уровне научных и прикладных работ с использованием методик нейтронного рассеяния. КЗ будет входить в состав комплекса нейтронных замедлителей на реакторе ИБР-2 /1-8/.

Установка КЗ включает в себя собственно криогенный замедлитель - камеру, заполняемую рабочим веществом в виде замороженных шариков из смеси ароматических углеводородов (мезитилен + m-ксилол), систему приготовления шариков и заполнения ими камеры, замены рабочего вещества при выработке ресурса, систему охлаждения камеры и поддержания температуры шариков на уровне 30 К и другие, вспомогательные системы, обеспечивающие нормальную работу КЗ.

КЗ представляет собой весьма сложную техническую структуру, создание которой требует поэтапного решения конкретных методических и конструкторских задач. К первостепенным задачам относится обеспечение загрузки замороженных шариков в камеру замедлителя. Выбранный принцип загрузки - транспортировка шариков холодным гелием (40К -80 К) по протяженной пневмотрассе от специального дозирующего устройства до камеры. Проблема транспортировки состоит в отсутствии как экспериментальных, так и теоретических данных об упруго-пластических, адгезионных и трибологических свойствах твердого аморфного мезитилена (каковой является его 70% смесь с m-ксилолом), а также о движении одиночного шарика по цилиндрической широкой трубе с учетом трения качения и скольжения и отклонения от сферичности. Все это затрудняло расчет параметров пневмотранспортной системы и разработку дозирующего устройства. Поэтому проблему транспортировки надо было решать экспериментально – сначала на специальном лабораторном стенде для решения проблемы движения одиночного шарика /9-11/, и затем - при помощи стенда с прототипом криогенного замедлителя нейтронов. В данной работе он представлен как испытательный стенд криогенного замедлителя для исследования характеристик холодной трассы загрузки шариков твердых замороженных ароматических углеводородов (мезитилена, m-ксилола)».

Цель создания стенда и проведения научно-исследовательских работ на нем - обоснование принятого принципа доставки и загрузки рабочего вещества в камеру холодного замедлителя нейтронов на основе ароматических углеводородов и проверка работоспособности технологических систем.

В настоящее время на испытательном стенде криогенного замедлителя нейтронов реактора ИБР – 2М выполнены следующие работы:

- произведена загрузка камеры-имитатора на 30% (~300 мл шариков);
- проведена отладка технологической системы управления и контроля;
- выбран оптимальный температурный режим работы стенда;
- определена рабочая скорость гелия во внутренней трубе пневмотрассы;
- определена оптимальная скорости подачи шариков из дозирующего устройства;
- определено время полной загрузки камеры-имитатора.

Испытательный стенд криогенного замедлителя нейтронов

Пневмотрасса стенда замедлителя разработана и введена в эксплуатацию на 3-м канале экспериментального зала №2 реактора ИБР-2. Она представляет собой повторение основных узлов и системам пневмотрассы реального замедлителя **(рис.1)**.

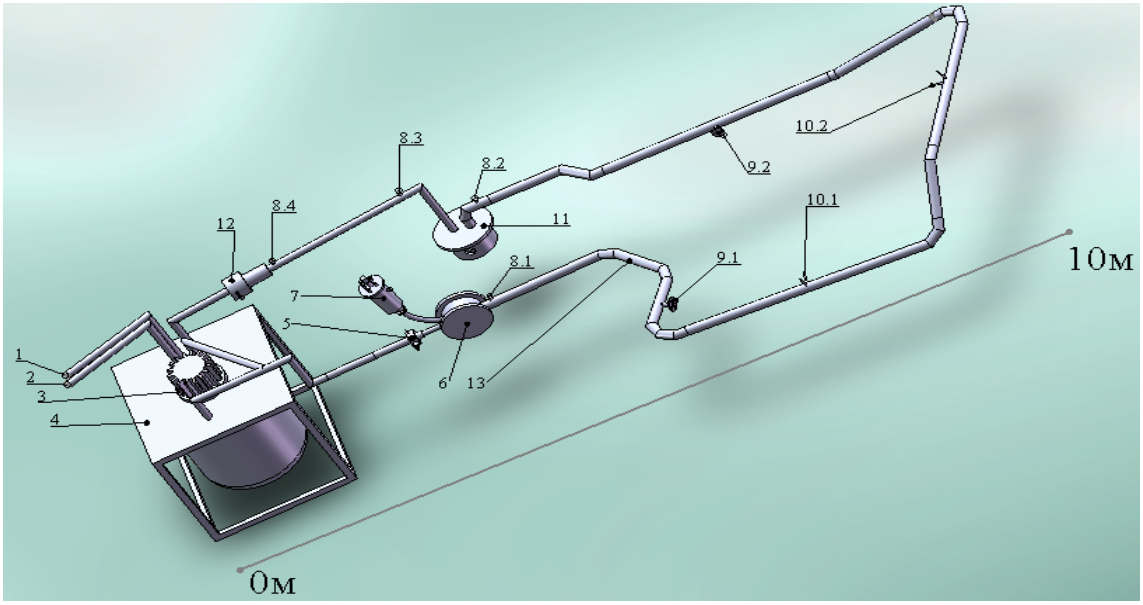

Рис.1. Трехмерный эскиз стенда криогенного замедлителя нейтронов реактора ИБР – 2М: 1-трубопровод подвода гелия к КГУ-500, 2- трубопровод отвода гелия от КГУ-500, 3-газодувка, 4-криостат, 5-узел с трубкой Пито и мановакуумметром, 6-тройник, 7-дозатор подачи шариков в пневмотракт; 8.1, 8.2, 8.3, 8.4-ТВО; 9.1, 9.2 - фланцы для откачки вакуума; 10.1, 10.2 - выводы трубок к датчикам движения шариков; 11- камера-имитатор холодного замедлителя, 12 - система подпитки гелия; 13-пневмотранспортный трубопровод.

Принцип работы стенда заключается в доставке замороженных шариков из дозатора к камере-имитатору по пневмотрассе с помощью холодного гелия при температуре 30-40К. Для подготовки стенда к работе, в межтрубном пространстве пневмотрассы (шарики транспортируются по внутренней трубе) и в криостате **(рис.2)** необходимо создать вакуум порядка 10^{-4} – 10^{-5} Torr.

Внутренний трубопровод откачивают через фланец дозатора шариков до получения форвакуума, с целью удаления воздуха и остатков мезитилена. После получения форвакуума трубопровод заполняют гелием комнатной температуры под давлением 1,03 атм. из газгольдера. Во время работы газгольдер постоянно открыт, благодаря чему давление гелия во внутренней трубе поддерживается на одном и том же уровне. Холодный гелий по трубопроводу его подвода от криогенной гелиевой машины (КГУ-500) поступает в криостат, после чего происходит захолаживание его первого контура. Значения температуры в криостате фиксируются датчиками типа ТВО (Т1-Т5, **рис.2**) и контролируются при помощи компьютера. После заполнения пневмотранспортного трубопровода гелием, он начинает циркулировать по пневмотрассе (2-ой контур криостата). Благодаря теплообменнику, температура гелия 2-го контура понижается, постепенно захолаживая внутреннюю трубу.

Температура на разных участках пневмотрассы фиксируется с помощью ТВО Т6-Т9. После получения рабочих температур 30-40К, можно переходить к процессу загрузки камеры-имитатора. Замороженные шарики, помещают в дозатор, который доставляет их во внутреннюю трубу пневмотрассы. Потоком холодного гелия шарики транспортируются к камере-имитатору, их появление в камере фиксируются Web-камерой. После окончания эксперимента, жидкий мезитилен удаляется из камеры-имитатора через специальную трубку.

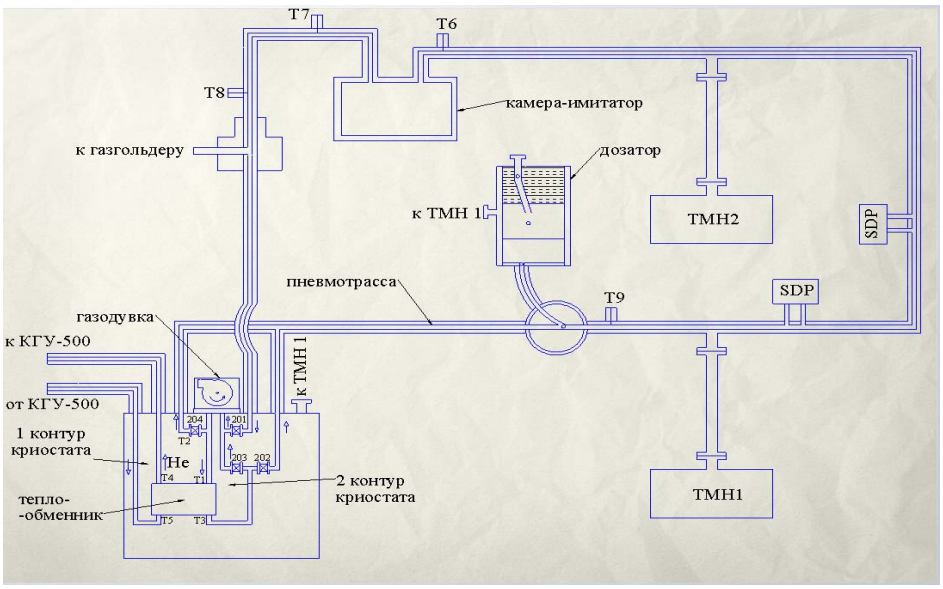

Рис.2 Технологическая схема стенда криогенного замедлителя нейтронов: ТМН и ФВН – турбомолекулярные и фор-вакуумные насосы, SDP – датчики дифференциального давления, Т – датчики температуры типа ТВО, 201-204 – вентили, регулирующие движение гелия в криостате

Технологическая система управления и контроля испытательного стенда криогенного замедлителя

На данный момент разработка системы управления и контроля стенда завершена **(рис.3)**, проводится ее отладка и оптимизация работы. Все модули системы объединены в единый блок, расположенный в экспериментальном зале, а управление и сбор данных осуществляется дистанционно с помощью ПК и специально написанного программного обеспечения.

Система управления и контроля включает в себя:

- модули контроля температуры и вакуума,
- модуль управления газодувкой (циркулятором гелия),
- модуль управления двигателем дозирующего устройства,
- модуль управления Web-камерой.

Система контроля температуры

Для контроля температуры используется комплекс из 8-ми последовательно соединенных датчиков типа ТВО (Т1-Т9, **рис.1**). Диапазон измеряемых температур составляет 15К-273К, что соответствует изменению сопротивления датчиков в диапазоне - 1,8кОм – 800Ом. Зависимость сопротивления от температуры – обратная.

Требуемая точность измерения температуры - 0,1град. Датчики подключены по 4-х проводной схеме, т.е. по 2-м проводам подводится постоянный ток, а через 2 других провода осуществляется съем напряжения, пропорционального измеряемой величине – сопротивлению датчика. Для регистрации напряжений с датчиков был выбран 8-канальный измеритель аналоговых сигналов ТМ 5103, который используется в режиме циклического просмотра измерений по всем 8 каналам на основном 4-х разрядном табло. Измеритель ТМ 5103 имеет интерфейс связи с ПК – RS232, что делает возможным его подключение к ПК по линии связи длиной до 15 м.

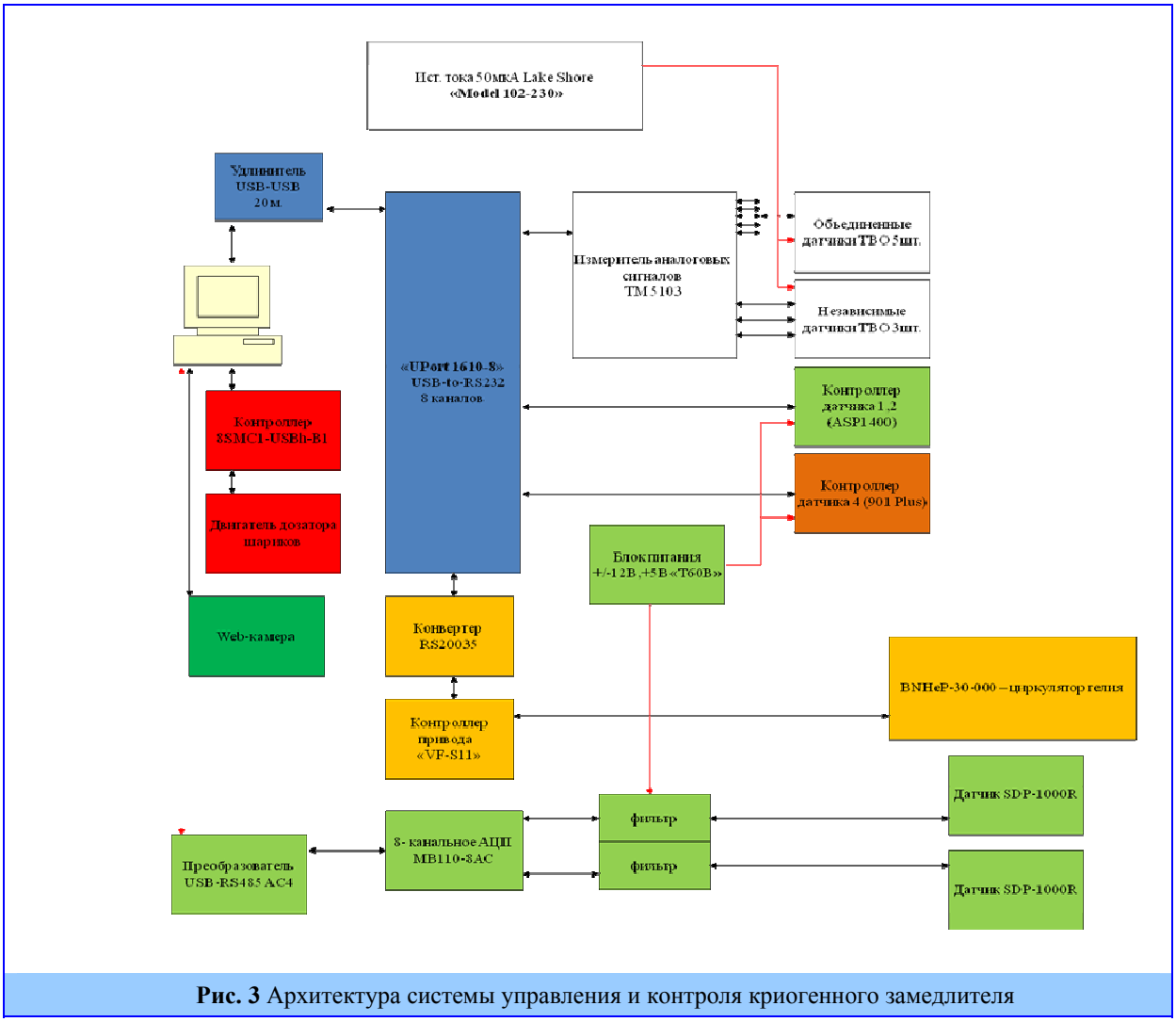

Рис. 3 Архитектура системы управления и контроля криогенного замедлителя

Система управления газодувкой (циркулятором гелия)

Газодувка (циркулятор гелия) предназначена для получения необходимой скорости движения рабочего газа во внутренней трубе. От скорости движения газа зависит скорость движения шариков по трубе, и, соответственно, время заполнения камеры макета. С одной стороны, скорость движения шариков не должна быть слишком большой, иначе они будут разрушаться, а с другой стороны, – не слишком малой, так как в этом случае время загрузки будет непозволительно большим. Характеристикой циркулятора, задающей скорость движения газа в трубе является частота вращения двигателя. В качестве частотного привода было выбрано устройство «VF-S11» фирмы Toshiba для двигателей мощностью до 400Вт.

Система управления двигателем дозирующего устройства

Дозирующее устройство («Дозатор») представляет собой цилиндр с диском у основания, на котором располагаются замороженные шарики **(рис.5)**. Цилиндр окружен вакуумно-азотной «рубашкой», предотвращающей приток тепла к диску с шариками **(рис.4)**. Верхний фланец «рубашки» имеет в верхней части специальное отверстие, через которое происходит загрузка. Диск соединен длинным штоком с шаговым электродвигателем.

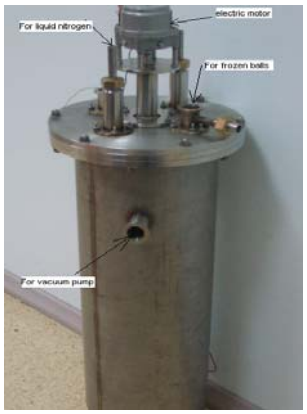

Рис.4 Дозирующее устройство

Рис.5 Цилиндр с диском

В качестве основы для системы управления дозатором шариков были выбраны контроллеры управления шаговыми двигателями фирмы Standa: 8SMC1- USBh-B1. Они позволяют в широком диапазоне регулировать скорость шагового двигателя. Для обеспечения плавности хода дозатора шаговый двигатель выбран с редуктором 1:150, что обеспечивает от нескольких оборотов в минуту до 1 оборота за несколько минут. Управление и контроль параметров работы, таких как положение, ускорение/замедление, скорость и направление движения осуществляется с персонального компьютера через USB интерфейс.

Система управления Web-камерой

Для контроля заполнения камеры макета используется Web-камера, которая в он-лайн режиме фиксирует попадание шариков внутрь камеры, через специальные стеклянные вставки **(рис.6)**

Рис. 6 Камера-имитатор макета

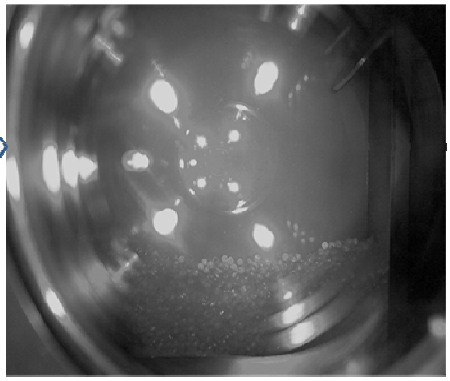

Рис. 7 Снимок шариков, сделанный Web-камерой

Web-камера записывает и передает изображение на компьютер через USB удлинитель, благодаря чему, пользователь может аблюдать за процессом загрузки шариков в режиме реального времени **(рис.7)**.

Заключение

На данный момент на макете криогенного замедлителя был проведен ряд экспериментов по загрузке камеры-имитатора. В ходе экспериментов в камеру было загружено около 300 мл шариков из необходимого количества в 1000 мл **(рис.7)**, был выбран оптимальный температурный режим работы, проведена отладка системы управления и контроля, оптимизация режимов загрузки, в частности, выбор скорости гелия во внутренней трубе, выбор скорости подачи шариков из дозатора, а также определено примерное время загрузки камеры. В ближайшее время планируются эксперименты по полной загрузке камеры, разработка системы подсчета количества шариков и

контроля возможных заторов шариков в трубе, а также выработка рекомендаций по эксплуатации реального криогенного замедлителя нейтронов.

Литература

1. С.А. Куликов, Е.П. Шабалин. Сравнение эффективности материалов холодных замедлителей нейтронов для реактора ИБР-2. Сообщение ОИЯИ Р17-2005-222.
2. S. Kulikov, E. Shabalin. Complex of neutron moderators for the IBR-2M reactor . In: Proceedings of 17th Meeting of the International Collaboration on Advanced Neutron Sources, ICANS-XVII. April 25-29, 2005. Santa Fe, New Mexico.
3. S. Kulikov, E. Shabalin. New complex of moderators for condense matter research at the IBR-2M reactor. Romanian Journal of Physics, ISSN:1221-146X, Изд:Publishing House of the Romanian Academy, V.54, 3-4, January.2009
4. Е.П. Шабалин, С.А. Куликов, В.В. Мелихов. Study of fast neutron irradiation effects in cold moderator materials. Письма в ЭЧАЯ N5 [114] 2003 стр. 82-88.
5. Е.П. Шабалин, Е.Н. Кулагин, С.А. Куликов, В.В. Мелихов Радиационные эксперименты с водородсодержащими материалами на криогенной облучательной установке УРАМ-2 реактора ИБР-2. Атомная Энергия т. 97, вып. 3, стр. 183-189, 2004
6. И. М. Баранов, И.И. Воронин, В.Г. Ермилов, Е.Н. Кулагин, С.А. Куликов, В.В. Мелихов, Р.Г. Пушкарь, Ро Ду Мин, Д.Е. Шабалин, Е.П. Шабалин. Изучение процесса выхода радиолитического водорода из экспериментального элемента холодного замедлителя на твердом мезитилене. Сообщения ОИЯИ, Р3-2004-212 (2004)
7. Е.Н. Кулагин, С.А. Куликов, В.В. Мелихов, Е.П. Шабалин. Radiation effects in cold moderator materials: Experimental study of accumulation and release of chemical energy. Nuclear Inst. and Methods in Physics Research, B, 215, (2004), 181-186.
8. С.А. Куликов, И.В. Калинин, В.М. Морозов, А.Г. Новиков, А.В. Пучков, А. Н. Черников, Е.П. Шабалин. Измерение спектров холодных нейтронов на макете криогенного замедлителя реактора ИБР-2. Письма в ЭЧАЯ, 2010. Т.7, №1 (157), с.95-100.
9. Е. П. Шабалин. О нерегулярности движения шара при пневмотранспорте в трубе. Сообщение ОИЯИ Р 3-2008-67, 12 стр.
10. Е.Н. Кулагин, С.А. Куликов, Д.Е. Шабалин, Е.П. Шабалин, О.Г. Бузыкин, А.В. Казаков. О пневмотранспортировке твердых шариков холодного замедлителя нейтронов. Сообщение ОИЯИ Р13-2008-116, 16 стр.
11. М.В.Булавин, Е.Н.Кулагин, С.А.Куликов, К.А.Мухин, Д.Е.Шабалин, Е.П.Шабалин. Моделирование пневмотранспорта твердых шариков холодного замедлителя нейтронов: распределение скорости и времени движения.. Сообщение ОИЯИ, Р13-2009-72, 16 стр.

EPITHERMAL NEUTRON ACTIVATION ANALYSIS OF THE ASIAN HERBAL PLANTS

Baljinnyam N., Jugder B[1]., Norov N[2]., Frontasyeva M.V., Ostrovnaya T.M., S.S. Pavlov

Frank Laboratory of Neutron Physics, JINR, Dubna
[1]Medical college "Monos", Ulaanbaatar, Mongolia
[2]Centre of Nuclear Research, NUM, Ulaanbaatar, Mongolia

Introduction

Herbal medicines are the staple of medical treatment in many civilizations including those of Africa, China, Egypt, India, Latin America and others (Steiner., R. P. 1986). According to the World Health Organization (WHO) estimates, 70% of the world population use herbal medicines and herbal products for primary health care (British Medical Association., 1993). Thousands of plants are used for curing various diseases in Mongolia. The larger part of treatment in Mongolian Traditional Medicine is medication. Mongolia has over 600 types of medical plants so far discovered. In addition Mongolia imports more than 100 components of traditional medicine from China and the Russian Federation (Ligaa. U., et.al., 1997).

Neutron activation analysis is a very convenient method for analyzing trace elements in all types of samples, including herbal medicine. Examples of recent work on the use of the technique are 28 elements in medicinal herbs (Sarmani S., et.al., 1998), 6] 12 elements in Chinese medicinal herbs (Yamashita C. I. et.al., 2005).

The present study was undertaken to investigate the elemental contents in 2 types of medicinal herbs commonly used in controlling and healing of different diseases.

Asian medicinal herbs Chrysanthemum (*Spiraea aquilegifolia* Pall.) and Red Sandalwood *(Pterocarpus Santalinus*) are widely used in folk and Ayurvedic medicine for healing and preventing some diseases. The modern medical science has proved that the Chrysanthemum (*Spiraea aquilegifolia* Pall.) possesses the following functions: reducing blood press, dispelling cancer cell, coronary artery's expanding and bacteriostating and Red Sandalwood *(Pterocarpus Santalinus*) is recommended against headache, toothache, skin diseases, vomiting and sometimes it is taken for treatment of diabetes. Species of Chrysanthemums were collected in the north-eastern and central Mongolia, and the Red Sandalwood powder was imported from India. Samples of Chrysanthemums (branches, flowers and leaves) (0.5 g) and red sandalwood powder (0.5 g) were subjected to the multi-element instrumental neutron activation analysis using epithermal neutrons (ENAA) at the IBR-2 reactor, Frank Laboratory of Neutron Physics (FLNP) JINR, Dubna. A total of 41 elements (Na, Mg, Al, Cl, K, Ca, Sc, V, Cr, Mn, Fe, Co, Ni, Zn, As, Se, Br, Rb, Sr, Zr, Mo, Cd, Cs, Ba, La, Hf, Ta, W, Sb, Au, Hg, Ce, Nd, Sm, Eu, Tb, Dy, Yb, Th, U, Lu) were determined. For the first time such a large group of elements was determined in the herbal plants used in Mongolia. The quality control of the analytical results was provided by using certified reference material Bowen Cabbage.

Experimental

Sample collection and preparation

Species of Chrysanthemums were collected in the north-eastern and central Mongolia, and the Red Sandalwood powder was imported from India. In the laboratory the sample of Chrysanthemums was cleaned from extraneous plant materials and dried to constant weight at 30^0-40^0 for 48 hours. The samples were not washed and not homogenized.

Chrysanthemum (*Spiraea aquilegifolia* Pall.)

Red Sandalwood *(Pterocarpus Santalinus*)

Analysis

The concentration of elements in the herbal plant samples was determined by a multi-element instrumental neutron activation analysis using epithermal neutrons (ENAA) at the IBR-2 reactor, FLNP JINR, Dubna (Frontasyeva M.V. et. al., 2000). To carry out ENAA investigations, plant samples of 0.5 g were heat-seated in polyethylene foil bags and packed in aluminum cups for short and long irradiation, respectively. The processing of the data and determination of the concentrations of elements were performed using certified reference materials and flux comparators with the help of the software developed in FLNP, JINR (Ostrovnaya T. M., et. Al., 1993)

Results and discussion

The concentrations of 41 elements were determined in 2 medicinal herbs samples using INAA. For the first time such a large group of elements was determined in the herbal plants used in Mongolia. The quality control of the analytical results was provided by using certified reference material Bowen Cabbage. The results obtained are compared to the "Reference plant" (B. Markert, 1992) data and interpreted in terms of excess of such elements as Se, Cr, Ca, Fe, Ni, Mo, and rare earth elements.

Conclusion

The data obtained in the present work are important for synthesis of new herbal drugs which can be used for the control and cure of various diseases. In order to develop a stronger basis for appreciating the curative effects of medicinal plants, there is a need to investigate their elemental content. It has been demonstrated that INAA with its multi-elemental characterization over a wide range of concentrations, blank free-nature and minimum sample preparation is the ideal analytical technique for such studies.

The authors acknowledge the financial assistance of the RFBR-Mongolia grant 08-05-90214-Mong_a.

References:

British Medical Association, Complementary Medicine: New Approaches to Good Practice, Oxford University Press, Oxford, 1993.

Frontasyeva M. V., Pavlov S. S., Analytical Investigations at the IBR-2 Reactor in Dubna, JINR Preprint, E14-2000-177, Dubna, 2000.

Ligaa U., et.al., Methods of uses of medicinal plants in Mongolian Traditional medicine and prescriptions. Artist Publishing, Ulaanbaatar: 1997, p. 9–10.

Markert B. Establishing of "Reference plant" for inorganic characterization of different plant species by chemical fingerprinting, // J. Water, Air, and Soil Pollution, Vol. 64, 1992, p. 533-538.

Ostrovnaya T. M., Nefedyeva L. S., Nazarov V. M., Borzakov S.B., Strelkova L. P., Software for INAA on the Basis of Relative and Absolute Methods Using Nuclear Data Base, Activation Analyisi in Enviroment Protection, D-14-93-325, Dubna, 1993, 319-326.

Sarmani S., Abugassa I., Hamzan A., // J. Radioanal. Nucl. Chem., 234, 1998, p. 17.

Steiner R. P. (Ed.) Folk Medicine – The Art and the Science, American Chemical Society, Washington DC, 1986, p. 223.

Yamashita C. I., Saiki M., Vasconcellos M. B. A., Sertie J. A. A., // J. Appl. Rad. Isotopes, 63, 2005, p. 841.

RADIOMETRY OF ^{137}CS AND ^{210}PB IN MOSS FROM BELARUS

Aleksiayenak Yu. V.[1], Frontasyeva M.V.[1], Florek M.[2], Faanhof A.[3]

[1]Frank Laboratory of Neutron Physics, Joint Institute for Nuclear Research, Dubna, Russia,
[2]Dept.of Nuclear Physics and Biophysics, Comenius University, Bratislava, Slovakia,
[3]South African Nuclear Energy Corporation, Pretoria, Republic of South Africa

Introduction

Mosses have been extensively used to study atmospheric deposition of trace metals on the European scale (Harmens et al, 2010), and they are equally suitable indicators of airborne radionuclides (Mattson, 1972; Sumerling, 1984; Barci-Funel, 1992; Steinnes and Njåstad, 1993; Nifontova, 1996, 1998; Sawidis, 1997; Florek, 2001; Popovic, 2008; Cevik and Celik, 2009). The south-eastern part of Belarus was severely contaminated with fallout from the 1986 accident at the Chernobyl nuclear power plant. About 70% of the total radioactive fallout occurred on Belarus territory (Kenik, 1995). Soil contamination with ^{137}Cs, ^{90}Sr and ^{239}Pu is still high, and eight years after the accident 2,640 km^2 of agricultural land was still excluded from use. Within the 40-km radius of the power plant, 2,100 km^2 of land in the Poles'e state nature reserve has been excluded from use for an indefinite period of time. Vast territories in the Gomel and Mahilyow regions were rendered uninhabitable. Roughly 7,000 km² of soil were contaminated by ^{137}Cs to levels greater than 550 GBq/km², i.e. inaccessible for human usage for a very long time. In 1995 the areas contaminated to ^{137}Cs levels exceeding 37 GBq/km² (1 Ci/km²) constituted about 23% of the country (IAEA, 2006) and in 2002 more than 1.5 million people still lived in this area.

Experimental

Sampling and sample preparation. Sixty-three samples of the moss species *Hylocomium splendens* and *Pleurozium schreberi* were collected in Belarus (Fig. 1) in order to study deposition of airborne radionuclides.

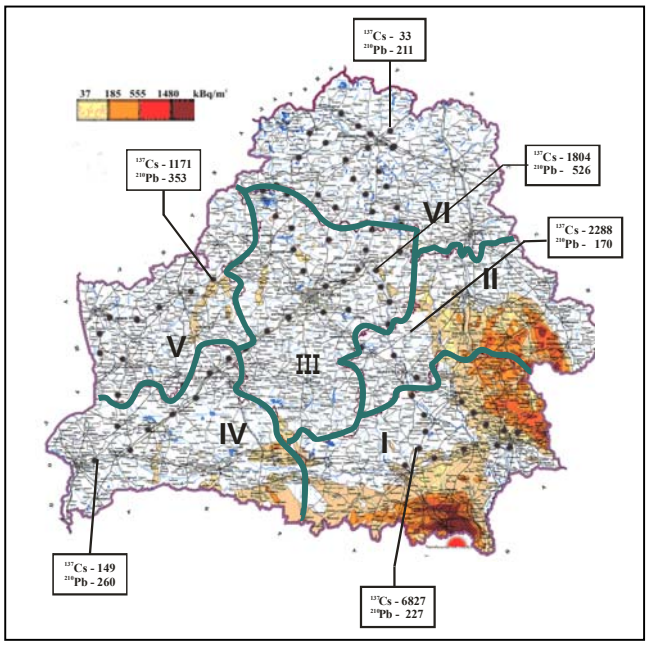

Fig. 1. Map of ^{137}Cs contamination in Belarus in 2004. with sampling sites. Maximum concentrations (Bq/kg) in different regions are given in squares

The sampling network in Belarus covers strongly contaminated (Gomel and Mahilyow) as well as relatively "clean" (Minsk, Grodno, Vitebsk) regions. Samples were dried and then pelletized prior to activity measurements. Sample weight of sample was typically around 17 gram, cylindrical geometry with height ca. 2–3 cm, and diameter about 7 cm.

Measurements. Gamma spectrometry on the moss samples was performed in the low-level background counting laboratory of the Department of Nuclear Physics and Biophysics of the Comenius University in Bratislava, Slovakia, using a Canberra

HPGe detector (177 cm^3) with a carbon window, placed in a low-level background shield. The measuring time was 24 hours or more. The counting statistics was less than 3%. The total uncertainty in determination of radionuclide activities was estimated at 15% or less. A limited suite of samples was also measured at the South African Nuclear Energy Corporation (SANEC) using an ultra low level background counting facility (160 cm3 n-type HPGe Canberra BE5030 detector mounted in a lead shield of 13 cm lead of less than 50 Bq/kg and another layer of 2 cm less than 10 Bq/kg lined with 1 mm cadmium, 2 mm copper and 4 mm Perspex). Measuring time was one hour. Data obtained in the two laboratories for samples from two localities in Belarus was compared and the results appear to be in agreement within experimental errors.

Results and Discussion

In Belarus the maximum activity of ^{137}Cs (6827 Bq/kg) was observed in the Gomel Region near the town Mazyr and the minimum one (4,83 Bq/kg) in Vitebsyevskii Region near Luzhki-Yazno. "Hot spots" were observed near town of Borisow and Yuratsishki. The ^{137}Cs activity in the moss presumably reflects the initial deposition of ^{137}Cs fallout from the Chernobyl accident. The obtained results support previous data showing particularly high deposition of ^{137}Cs in the Gomel and Mahilyow Regions from the Chernobyl accident (IAEA, 2006). Most radionuclides, deposited on soil, are located in its top layers. ^{137}Cs migration deep into the soil occurs very slowly. The median value of concentrations of ^{137}Cs in the samples from Gomel and Mahilyow regions are in ten-twenty times higher compared to other Belarus regions. The main reason why the moss samples still reflect the original distribution of Chernobyl fallout in Belarus is probably that Cs migrates progressively from the older to the younger shoots, as shown in studies of moss samples exposed to Chernobyl fallout in Norway (Gaare and Steinnes, 1996).

The results obtained in the present study confirm the spatial distribution of ^{137}Cs in Belarus due to fallout from the Chernobyl accident.

The median value of ^{137}Cs concentrations in moss samples from Gomel and Mahilyow regions are more ten times higher than present values from other Belarus regions and literature values from the outside territories (see Fig. 2) where corresponding studies have been carried out. The minimum concentrations in Belarus however are similar to those reported from the other studies. The concentrations of ^{210}Pb in moss samples collected over the territory of Belarus vary within the range 141–575 Bq/kg with a median value of 312 Bq/kg. In comparison with concentration of ^{137}Cs the range is narrow, and

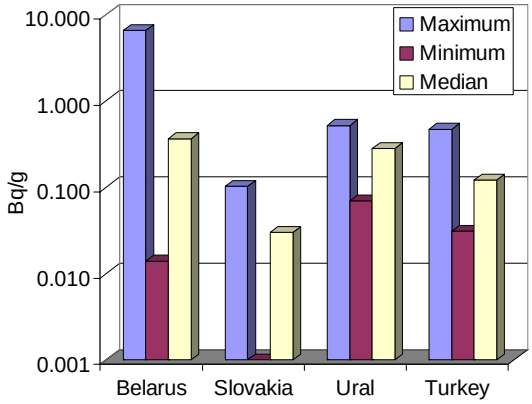

Fig. 2. Comparison of ^{137}Cs concentration in moss from different countries

differences between regions are small from region to region.

References

Barci-Funel, G., Dalmasso, J., Ardisson, G., 1992. Deposition of long-lived radionuclides after the Chernobyl accident in the forestal massif of Boreon. J. radioanal. nucl. chem. 164, 157-169

Berg, T., Steinnes, E., 1997. Use of mosses (Hylocomium splendens and Pleurozium schreberi) as biomonitors of heavy metal deposition: from relative to absolute values. Environmental Pollution. 98, 61-70.

Cevik, U., Celik, N., 2009. Ecological half-life of ^{137}Cs in mosses and lichens in the Ordu province, Turkey by Cevik and Celik. J. Environ. Radioact. 100, 23-28.

Florek, M., Frontasyeva, M., Mankovska, B., Oprea, K., Pavlov, S., Steinnes, E., , 2001. Air pollution with heavy metals and radionuclides in Slovakia studied be the moss biomonitoring technique. ISINN-9, 442-449.

Gaare, E., Steinnes, E., 1996. Use of the moss Hylocomium splendens for the mapping of radiocaesium fallout from the atmosphere. Proceedings, Nordic Radioecology Seminar, Reykjavik, 26-29 August, 367-370.

Harmens, H. et al., 2010. Mosses as biomonitors of atmospheric heavy metals deposition: Spatial patterns and temporal trends in Europe. Environmental Pollution. 158, 3144-3156.

IAEA, 2006. International Atomic Energy Agency, Environmental Consequences of the Chernobyl Accident and their Remediation: Twenty Years of Experience. Report of the UN Chernobyl Forum Expert Group "Environment". In: Radiological Assessment Reports Vienna.

Kenik, I., 1995. Belarus: a small country faces 70 percent of the fallout. DHA News. September-October, 7-8

Kulan, A., 2006. Seasonal ^{7}Be and ^{137}Cs activities in surface air before and after the Chernobyl event. Journal of Environmental Radioactivity. 90, 140-150.

Mattsson, S., 1972. Radionuclides in Lichen, Reindeer and Man. Lund, 48.

Nifontova, M., 1996. Mushrooms, lichens and mosses as biological indicators of radioactive environmental contamination. Radioecology and the restoration of radioactive-contaminated sites. 155-162.

Nifontova, M., 1998. Content of long-lived artificial radionuclides in moss-lichens cover of terrestrial ecosystems of the Ural-Siberian Region. Ecology 3, 196-200 (in Russian).

Popovic, D. et al, 2008. Radionuclides and heavy metals in Borovac, Southern Serbia. Environ. Sci. Pollut. Res. 15, 509-520.

Povinec, P., Chudy, M., Sýkora, I., Szarka, J., Pikna, M., Holý, K., 1988. Aerosol radioactivity monitoring in Bratislava following the Chernobyl accident. J. Radioanal. Nucl. Chem. Letters 126/6, 467-478.

Sawidis, Th., Heinrich, G., Chettri, M., 1997. Cesium-137 monitoring using mosses from Macedonia, N. Greece. Water, Air and Soil Pollution. 110, 171-179.

Steinnes, E., Njåstad, O., 1993. Use of mosses and lichens for regional mapping of ^{137}Cs fallout from the Chernobyl accident. J. Environ. Radioact. 21, 65-73.

Sumerling, T., 1984. The use of mosses as indicators of airborne radionuclides near a major nuclear installation. The Science of the Total Environment. 35, 251-265.

UNSCEAR, 1982. United Nations Scientific Committee on the Effects of Atomic Radiation Report. Ionizing Radiation: Sources and Biological Effects, United Nations, New York.